

Calorimetry at a Future Linear Collider

Steven Green
of Emmanuel College

A dissertation submitted to the University of Cambridge
for the degree of Doctor of Philosophy

Abstract

This thesis describes the optimisation of the calorimeter design for collider experiments at the future Compact Linear Collider (CLIC) and the International Linear Collider (ILC). The detector design of these experiments is built around high-granularity Particle Flow Calorimetry that, in contrast to traditional calorimetry, uses the energy measurements for charged particles from the tracking detectors. This can only be realised if calorimetric energy deposits from charged particles can be separated from those of neutral particles. This is made possible with fine granularity calorimeters and sophisticated pattern recognition software, which is provided by the PandoraPFA algorithm. This thesis presents results on Particle Flow calorimetry performance for a number of detector configurations. To obtain these results a new calibration procedure was developed and applied to the detector simulation and reconstruction to ensure optimal performance was achieved for each detector configuration considered.

This thesis also describes the development of a software compensation technique that vastly improves the intrinsic energy resolution of a Particle Flow Calorimetry detector. This technique is implemented within the PandoraPFA framework and demonstrates the gains that can be made by fully exploiting the information provided by the fine granularity calorimeters envisaged at a future linear collider.

A study of the sensitivity of the CLIC experiment to anomalous gauge couplings that effect vector boson scattering processes is presented. These anomalous couplings provide insight into possible beyond standard model physics. This study, which utilises the excellent jet energy resolution from Particle Flow Calorimetry, was performed at centre-of-mass energies of 1.4 TeV and 3 TeV with integrated luminosities of 1.5ab^{-1}

and 2ab^{-1} respectively. The precision achievable at CLIC is shown to be approximately one to two orders of magnitude better than that currently offered by the LHC.

In addition, a study into various technology options for the CLIC vertex detector is described.

Declaration

This dissertation is the result of my own work, except where explicit reference is made to the work of others, and has not been submitted for another qualification to this or any other university. This dissertation does not exceed the word limit for the respective Degree Committee.

Steven Green

Acknowledgements

Of the many people who deserve thanks, some are particularly prominent, such as my supervisor. . .

Contents

1	Energy Estimators	1
1.1	Motivation	1
1.2	Calibration in the Particle Flow Paradigm	4
1.2.1	Overview of the Calibration Procedure	5
1.2.2	MIP Scale Determination in the Digitiser	6
1.2.3	Digitisation Implementation	6
1.2.3.1	ECal Digitisation Implementation	6
1.2.3.2	HCal Digitisation Implementation	8
1.2.3.3	HCal Ring Digitisation Implementation	10
1.2.4	MIP Scale Determination in PandoraPFA	11
1.2.5	Electromagnetic Scale in PandoraPFA	12
1.2.6	Hadronic Scale in PandoraPFA	14
1.2.7	Summary	17
1.3	Novel Energy Estimators	18
1.3.1	HCal Hit Energy Truncation	19
1.3.1.1	Legacy Energy Corrections	20
1.3.1.2	Impact on Single Particle Energy Resolution	20
1.3.1.3	Impact on Jet Energy Resolution	21
1.3.2	Software Compensation	23
1.3.2.1	Impact on Single Particle Energy Resolution	27
1.3.2.2	Impact on Jet Energy Resolution	27
1.3.3	Summary	30
1.4	Timing Cuts	30
1.4.1	Impact on Single Particle Energy Resolution	32
1.4.2	Impact on Jet Energy Resolution	33
1.4.3	Summary	34

2	Calorimeter Optimisation Studies	35
2.1	Introduction	35
2.2	Electromagnetic Calorimeter Optimisation	35
2.2.1	ECal Cell Size	37
2.2.2	ECal Longitudinal Sampling Frequency	40
2.2.3	ECal Active Material	41
2.3	Hadronic Calorimeter Optimisation	44
2.3.1	HCal Cell Size	45
2.3.2	HCal Number of Layers	48
2.3.3	HCal Longitudinal Sampling Frequency	51
2.3.4	HCal Sampling Fraction	54
2.3.5	HCal Absorber Material	55
2.4	Global Detector Parameters	59
2.4.1	The Magnetic Field Strength	60
2.4.2	Inner ECal Radius	63
2.5	Summary	65
	Bibliography	69

*“Writing in English is the most ingenious torture
ever devised for sins committed in previous lives.”*

— James Joyce

Chapter 1

Energy Estimators

“There, sir! that is the perfection of vessels!”

— Jules Verne, 1828–1905

1.1 Motivation

This section outlines a procedure for calibrating the Monte-Carlo (MC) response of the linear collider detector simulations with a focus on converting the detector response into accurate energy measurements, "energy estimators", for particles showering in the calorimeters. In the particle flow paradigm, all neutral particle energies are measured using the calorimeters, which makes accurate energy reconstruction crucial for determining detector performance. Additionally, comparisons of particle shower energy and charged particle track momenta govern the event reconstruction in PandoraPFA during the reclustering stage, which further emphasises the importance of reliable energy estimators.

The goal of a calorimeter is to measure the energy of particles that shower within it. Particle showers are a cascade of secondary particles that are produced as a high energy particle interacts with a dense material. The energy deposits produced by a showering particle in the calorimeter are referred to as hits. The number of hits created by a particle shower in a calorimeter depends upon the size and shape of the particle shower and the segmentation of the calorimeter. The energy of the showering particle, $E_{Cluster}$, is determined by grouping these energy deposits together into clusters and summing their

energy

$$E_{Cluster} = \sum_{ECal \text{ hits, } i} E_{ECal}^i + \sum_{HCal \text{ hits, } i} E_{HCal}^i , \quad (1.1)$$

where E_{ECal}^i is the energy of ECal hit i and E_{HCal}^i is the energy HCal hit i . In this example, the energy deposits are assumed to be split across an ECal and a HCal, therefore, the sum runs over the hits in both calorimeters. This naive energy estimator will act as a starting point for the development of more sophisticated procedures aimed at improving the energy resolution.

The linear collider detector concepts employ highly-granular sampling calorimeters [1, 2]. These calorimeters are comprised of alternating layers of active and absorber materials [3]. The absorber layers initiate particle showers and propagate their growth, while the active layers produce a signal that is proportional to the energy deposited within them. The signal produced in the active layers is measured by sampling calorimeters and used to estimate the energy deposited in the absorber layers. This estimation is made by assuming the energy deposited across a calorimeter hit, that is one active and one absorber layer, is uniform. Working under this assumption, the total calorimeter hit energy is proportional to the active layer hit energy. This estimation procedure is loosely referred to as digitisation and, in this way, the cluster energy estimator introduced above can be written as

$$E_{Cluster} = \sum_{ECal \text{ hits, } i} \epsilon_{ECal}^i \alpha_{ECal} + \sum_{HCal \text{ hits, } i} \epsilon_{HCal}^i \alpha_{HCal} , \quad (1.2)$$

where α_{ECal} and α_{HCal} are digitisation constants for the ECal and HCal respectively, ϵ_{ECal}^i is the ECal active layer hit energy for hit i and ϵ_{HCal}^i is the HCal active layer hit energy for hit i . The first stage of the calibration procedure presented in this chapter covers the determination of these digitisation constants, which convert the raw analogue-to-digital converter (ADC) response to a hit energy.

Once the basic energy estimator has been calibrated, it is possible to apply more advanced procedures designed to give a compensating calorimeter response [4]. A compensating calorimeter produces an identical response to a particle shower irrespective of whether the particle shower is electromagnetic or hadronic in nature. The primary cause of the difference in the response of a calorimeter to electromagnetic and hadronic showers is the undetectable energy component that is found in hadronic showers. These undetectable energy components are energy deposits produced from a showering particle that do

not produce a signal in the calorimeters. Hadronic showers contain this undetectable component due to a combination of effects such as neutrons stopping within the calorimeter and nuclear binding energy losses. Typically, this leads to calorimeters having a weaker response to hadronic showers than to electromagnetic showers.

There are two distinct routes available for achieving a compensating response from a calorimeter: the first is hardware compensation [5], whereby calorimeters are constructed using materials that yield extra energy in response to hadronic showers; and the second is software compensation [6], whereby the uncompensated calorimetric energies for hadronic showers are modified at the software level.

A novel example of hardware compensation is the ZEUS calorimeter [5]. The ZEUS calorimeter was constructed using uranium as the absorber material. In response to neutral hadrons the uranium undergoes fission producing extra energy that increases the hadronic response of the calorimeter. The amount of uranium was carefully chosen to achieve a fully compensating calorimeter response, i.e. identical calorimeter response to electromagnetic and hadronic showers. While hardware compensation is possible for the linear collider calorimeters, restrictions on calorimeter construction and the use of a large amount of radioactive material are highly undesirable.

The linear collider lends itself to software compensation as the fine segmentation of the calorimeters and precise reconstruction of individual particles makes identification of hadronic showers, and modifying their energies, feasible. A basic form of software compensation included in the linear collider reconstruction is the modification of the electromagnetic cluster energy estimator to

$$E_{EM\ Cluster} = \sum_{ECal\ hits, i} E_{ECal}^i \beta_{ECal}^{EM} + \sum_{HCal\ hits, i} E_{HCal}^i \beta_{HCal}^{EM}, \quad (1.3)$$

and the hadronic cluster energy to

$$E_{Had\ Cluster} = \sum_{ECal\ hits, i} E_{ECal}^i \beta_{ECal}^{Had} + \sum_{HCal\ hits, i} E_{HCal}^i \beta_{HCal}^{Had}, \quad (1.4)$$

where the β s are scaling factors that are applied to the energy of clusters of calorimeter hits associated with electromagnetic and hadronic clusters in the ECal and HCal. This simple scaling of energies compensates the response of the calorimeters, which leads to better detector performance. Determination of these energy scale setting constants is the second stage of the calibration procedure that is presented in this chapter.

While this scaling of energies improves detector performance, it does not account for any changes to the β scaling factors as a function of the total energy deposited. An energy dependence in the scaling factors is expected as the mechanisms governing the propagation of hadronic showers are sensitive to the shower energy [7]. To account for this, more sophisticated software techniques have been developed that vary the calorimeter cluster energy estimator as a function of energy to achieve a compensating response across a wider range of energies. These techniques make use of the fine segmentation of the linear collider calorimeters to identify hadronic showers. These techniques also address the problem of spuriously high energy calorimeter hits, which are caused by Landau fluctuations [8]. Landau fluctuations originate from high energy knock-on electrons appearing within particle showers [9] and can lead to overestimates of the particle shower energy if they occur in the active layers of a sampling calorimeter.

1.2 Calibration in the Particle Flow Paradigm

Calibration of the linear collider detector simulation is performed in two processors in the software framework; the digitiser, which performs the digitisation process for sampling calorimeters, and PandoraPFA. The input to the digitiser is the active layer calorimeter response (ADC values) and the output is the combined, active and absorber layer, calorimeter hit energies. The hit energies are then used by PandoraPFA for event reconstruction. Calibration of the digitiser involves determining the digitisation constants (α_{ECal} and α_{HCal}) and the minimum ionising particle (MIP) scale, which is the average energy response for a MIP on a per hit basis. Similarly, calibration of PandoraPFA requires setting the scaling factors, β , and the MIP response using the combined calorimeter hit energies.

The α and β constants are determined by tuning the mean of reconstructed energy distributions. A number of cuts are applied when populating these reconstructed energy distributions that ensure the relevant reconstructed energy is being tuned. The application of these cuts means that linear scaling of the α and β constants does not lead to a linear shift in the mean of the reconstructed energy distributions. Therefore, when calibrating the α and β constants an iterative approach is taken; the next iteration of the calibration constant is determined by repeating the reconstruction using the current iteration of the constant and adjusting the constant based on the mean of the reconstructed energy distribution.

Determining the MIP scale is included in the calibration procedure as it is used by PandoraPFA in the identification of muons and for applying energy thresholds designed to limit the impact of noise. This energy scale is also used by the digitiser when simulating electrical noise, saturation effects in scintillator readout technologies and for applying noise vetoing energy thresholds [10].

The, non-zero, peak in the distribution of hit energies and ADC values for normally incident 10 GeV μ^- events is used to define the MIP scale in PandoraPFA and the digitiser respectively [9]. In the linear collider detector simulation, several realistic effects are simulated by the digitiser including saturation effects, energy thresholds, timing cuts and electrical noise. Application of these effects at this point in the software chain means that the active layer hit energies are not subject to them, while the post digitisation combined calorimeter hit energies are. Consequently, the MIP scale in PandoraPFA cannot be obtained from the digitiser MIP scale, instead both have to be independently determined.

Although this overall procedure is referred to as calibration, strictly speaking this is not correct. Calibration sets the detector response to real data, while this procedure sets the simulated detector response to Monte-Carlo (MC) events. In a real detector, calibration would follow the setting of the simulated detector response to MC events so that simulations can be used to guide the calibration process.

1.2.1 Overview of the Calibration Procedure

The calibration procedure is split into four separate operations: determination of digitisation constants (α s) in the digitiser; determination of scaling factor constants (β s) in PandoraPFA; MIP scale setting in the digitiser; and MIP scale setting in PandoraPFA. Calibration of the digitiser, digitisation constants and MIP scale, uses calorimetric energy measurements prior to any reconstruction, while calibration of PandoraPFA, scale factors and MIP scale, uses fully reconstructed particle flow objects (PFOs). As reconstructed PFOs are created using calorimetric energy measurements that have been digitised, it is wise to calibrate the digitiser before PandoraPFA, therefore, the calibration procedure is applied in the following order:

1. Setting the MIP response in the digitiser.
2. Setting the digitisation constants, α s, in the digitiser.

3. Setting the MIP response in PandoraPFA.
4. Setting the scaling factors, β s, in PandoraPFA.

1.2.2 MIP Scale Determination in the Digitiser

The MIP scale in the digitiser was determined by simulating 10 GeV μ^- events and creating a distribution of active layer calorimeter hit energies for each calorimeter in the detector simulation. When populating these distribution, a direction correction factor of $\cos(\theta)$, where θ is the incident angle of the μ^- to the calorimeter cell, was applied to account for the path length of the MIP through the active medium of the calorimeter. This converts the individual response to a normal-incident equivalent response. No selection cuts were applied to the sample of muon events.

Figure 1.1 shows the distribution used to determine the MIP peak in the ECal, HCal barrel, HCal endcap and HCal ring. In the digitiser software only a single HCal MIP scale, taken as the HCal barrel, is implemented.

1.2.3 Digitisation Implementation

This section discusses how the digitisation constants, α s, are determined. The digitisation constant for a given calorimeter depends upon several factors such as the material properties of the active and absorber layers, the magnetic field strength and energy losses occurring within the gaps in the detector. Therefore, each calorimeter in the ILD detector model has a distinct constant that must be determined independently.

1.2.3.1 ECal Digitisation Implementation

The procedure for determining the digitisation constants in the ECal involves simulation of single photons at an energy $E_{MC} = 10$ GeV. Single photons at this energy are largely contained within the ECal, as shown in figure 1.2a. This makes them ideal for isolating the ECal digitisation calibration from that of the HCal digitisation calibration. Events are only used for calibrating the ECal digitisation if they are confined to the ECal. To that extent, cuts are applied ensuring that the sum of the reconstructed energy found outside the ECal is less than 1% of E_{MC} and that the $\cos(\theta) < 0.95$, where θ is the polar angle of the photon. Photons that convert are also vetoed in this event sample at MC

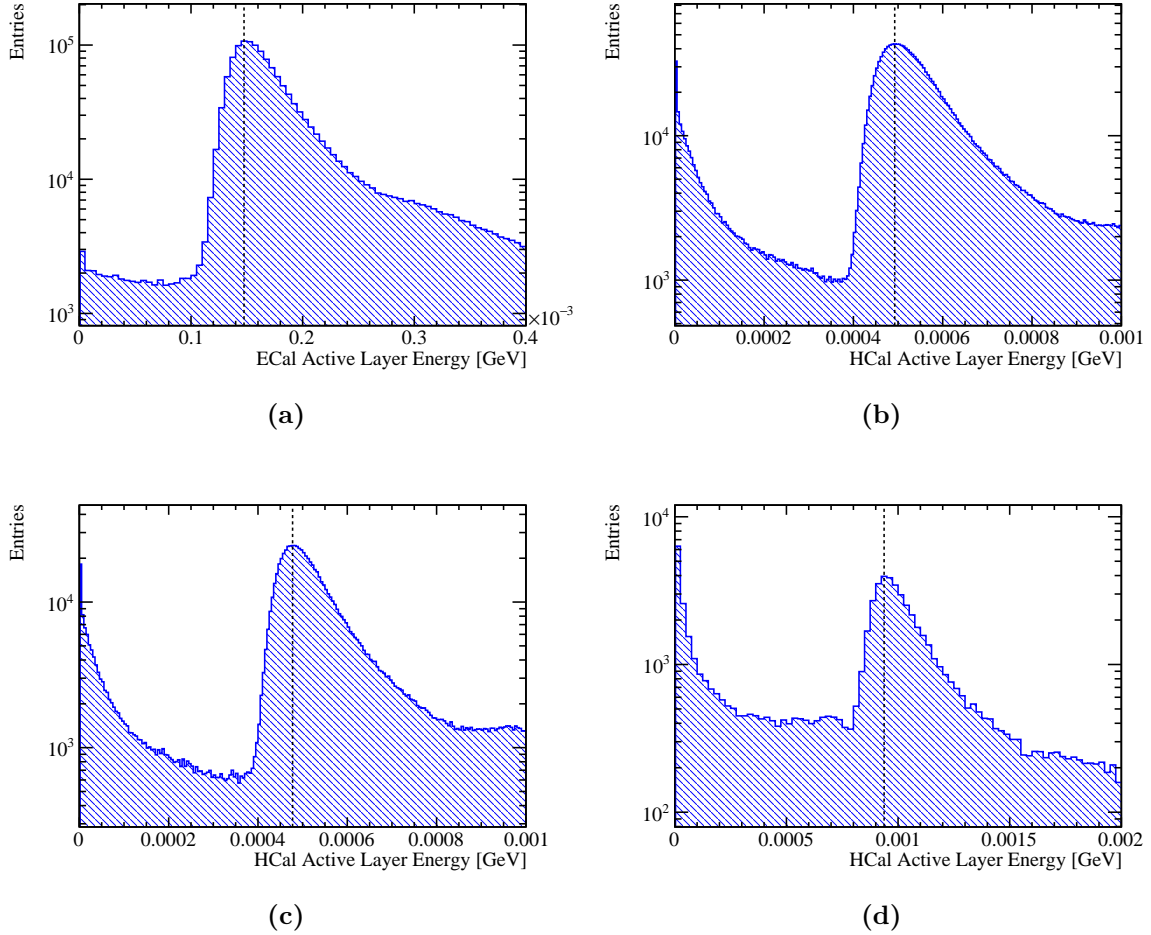


Figure 1.1: The active layer calorimeter hit energy distributions for (a) the ECal, (b) the HCal barrel, (c) the HCal endcap and (d) the HCal ring for 10 GeV μ^- events. The hit energies were corrected to account for the path length of the muons through the active medium of the calorimeter. The vertical black dotted lines indicate the position of the peak in each of these distributions that is used for defining the MIP scale in the digitisation processor.

level. The impact of these cuts on the sum of ECal hit energies for the $E_{MC} = 10$ GeV photons is shown in figure 1.2b.

The calibration of the digitisation in the ECal is an iterative procedure, which begins with the simulation of single photons using a trial calibration, α_{ECal}^0 . Next the distribution of the sum of calorimeter hit energies within the ECal is produced for events passing the selection cuts, as shown in figure 1.2b. For an ideal calorimeter this distribution should be Gaussian, as described in chapter 2, therefore, a Gaussian fit is applied to this distribution and the mean, E_{Fit} , extracted. To remove the effect of any outliers in this

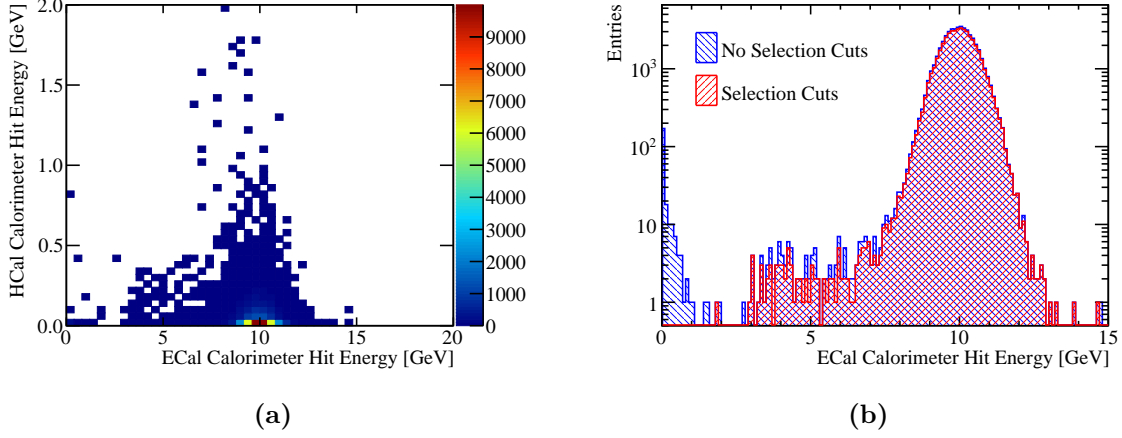


Figure 1.2: (a) The sum of calorimeter hit energies in ECal and HCal for 10 GeV photons. (b) The sum of the ECal calorimeter hit energies for 10 GeV photons with and without the selection cuts.

distribution, the fit is applied to the range of data with the smallest root mean square that contains at least 90 % of the data. An example of such a fit is shown in figure 1.3. In the case of ideal calibration, the mean of this fit, E_{Fit} , would be equal E_{MC} . It is assumed that any difference between the two is due to the calibration, therefore, to correct this the digitisation constant from the trial calibration, α_{ECal}^0 , is rescaled by the ratio of the E_{MC} to E_{Fit}

$$\alpha_{\text{ECal}}^0 \rightarrow \alpha_{\text{ECal}} = \alpha_{\text{ECal}}^0 \times \frac{E_{MC}}{E_{\text{Fit}}} . \quad (1.5)$$

This procedure is then repeated until the E_{Fit} falls within a specified tolerance of E_{MC} . The tolerance applied here was $|E_{\text{Fit}} - E_{MC}| < E_{MC} \times 5\%$. The binning used for the fitted histogram is chosen such that the bin width is equal to the desired tolerance on E_{Fit} e.g. $E_{MC} \times 5\% = 0.5$ GeV. It should be emphasised that the PFO energies used for downstream analyses have the electromagnetic and hadronic energy scale corrections applied, which are calibrated to a much tighter accuracy.

1.2.3.2 HCal Digitisation Implementation

The calibration for the digitisation in the HCal proceeds in a similar manner to that described for the ECal with a few key differences. This calibration uses simulated MC long-lived neutral kaons (K_L^0 s) at $E_{MC} = 20$ GeV. The higher energy, with respect to

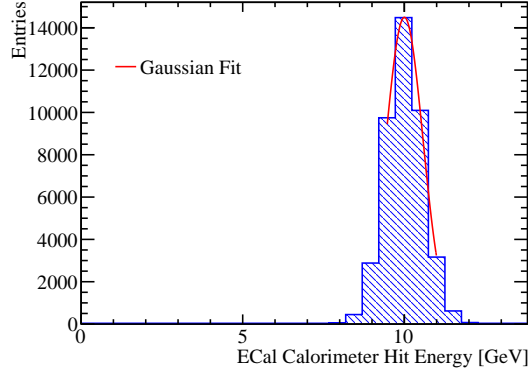


Figure 1.3: Gaussian fit to sum of the ECal calorimeter hit energies for 10 GeV photons with selection cuts. The coarse binning reflects the tolerance on the digitisation constant calibration.

the ECal digitisation, results in particle showers that sample deeper into the HCal. The K_L^0 s must pass through the ECal, which contains one λ_I , before arriving at the HCal. Consequently, approximately 15% of these events begin showering in the ECal, as can be seen in figure 1.4a. Only events that deposit less than 5% of their energy in the ECal are used for calibrating the HCal digitisation constants. Furthermore, events that are not contained in the HCal are removed by requiring the last layer of the HCal where energy is deposited is required to be in the innermost 90% of the HCal. The impact of these cuts on the sum of HCal calorimeter hit energies for the $E_{MC} = 20$ GeV K_L^0 events is shown in figure 1.4b.

There are two HCal digitisation constants used in the detector simulation, one applied for the barrel and another for the endcap. The use of two digitisation constants accounts for differences in hadronic shower dynamics between the two, such as differing magnetic field configurations in the barrel and endcap. Both parameters are calibrated in the same manner, but have different cuts on θ , the polar angle of the K_L^0 . For the barrel region of the HCal events are selected if $0.2 < \cos(\theta) < 0.6$, while for the endcap events are selected if $0.8 < \cos(\theta) < 0.9$. These angular cuts account for the transverse profile of the hadronic showers and ensure that the showers are largely confined to the relevant sub-detector. As many of the neutral hadrons appearing in jets are neutrons and their accessible energy is the kinetic energy as opposed to the total energy, the target reconstructed energy for these K_L^0 samples is the kinetic energy.

After applying the above K_L^0 selection cuts, the calibration procedure for the digitisation of the HCal barrel and endcap proceeds in the same manner as was described

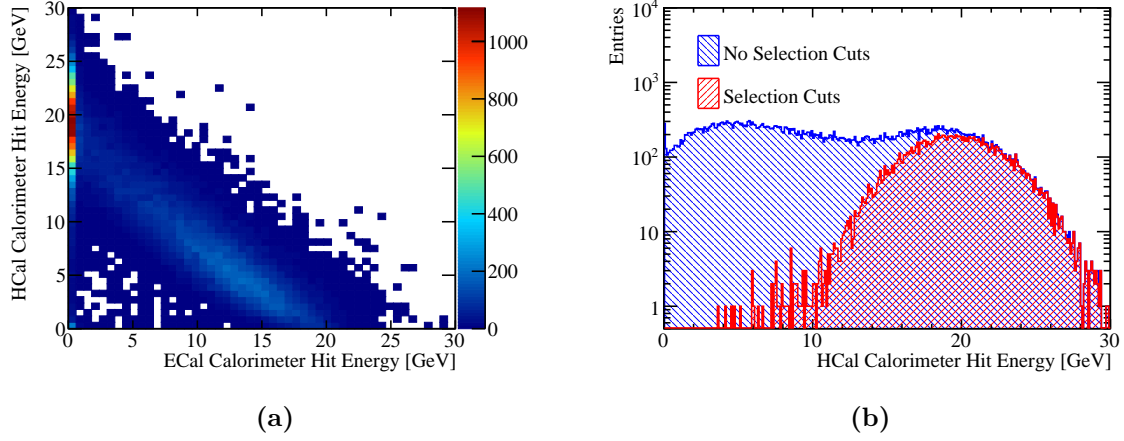


Figure 1.4: (a) Sum of calorimeter hit energies in ECal and HCal for 20 GeV K_L^0 events. (b) Sum of the HCal calorimeter hit energies for a 20 GeV K_L^0 events with and without the selection cuts.

for the ECal. An example of the Gaussian fits applied to the sum of the calorimeter hit energies in the HCal barrel and endcap are shown in figure 1.5.

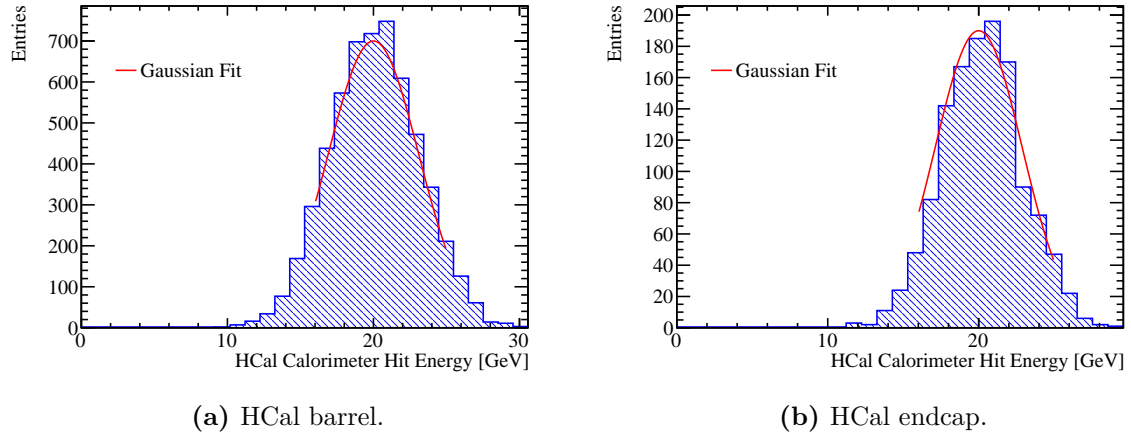


Figure 1.5: Gaussian fit to sum of the HCal calorimeter hit energies for 20 GeV K_L^0 events with selection cuts.

1.2.3.3 HCal Ring Digitisation Implementation

The HCal ring, as illustrated in figure 1.6, is a hadronic calorimeter that surrounds the ECal endcap and is sandwiched between the HCal barrel and endcap. This calorimeter

is required to ensure hermetic coverage of the hadronic calorimeter system across the barrel/endcap cross-over region [1].

The HCal ring has an independent digitisation constant to account for any difference in the hadronic shower development between the ring, barrel and endcap. Due to the thickness of the HCal ring, particle showers are never fully contained in it, so a different approach to calibration is required. To ensure that the HCal ring calibration is approximately correct, $\alpha_{\text{HCal ring}}$ is assumed to equal $\alpha_{\text{HCal endcap}}$ multiplied by several factors designed to account for differences in the active layer thickness, absorber layer thickness and the MIP response between the HCal endcap and ring. In detail

$$\alpha_{\text{HCal ring}} = \alpha_{\text{HCal endcap}} \times \frac{\langle \cos(\theta_{\text{endcap}}) \rangle}{\langle \cos(\theta_{\text{ring}}) \rangle} \times \frac{P_{\text{endcap}}}{P_{\text{ring}}} \times \frac{L_{\text{endcap}}^{\text{Absorber}}}{L_{\text{ring}}^{\text{Absorber}}} \times \frac{L_{\text{ring}}^{\text{Active}}}{L_{\text{endcap}}^{\text{Active}}}, \quad (1.6)$$

where θ is the incident angle of the incoming particle to the calorimeter determined using the 20 GeV K_L^0 s, L^{Active} is the active layer thickness and L^{Absorber} is the absorber layer thickness. P is the position of the MIP peak in the distribution of active layer hit energies, which has been corrected so that the MIP appears to enter the calorimeter at normal incidence, and is determined using 10 GeV μ^- events.

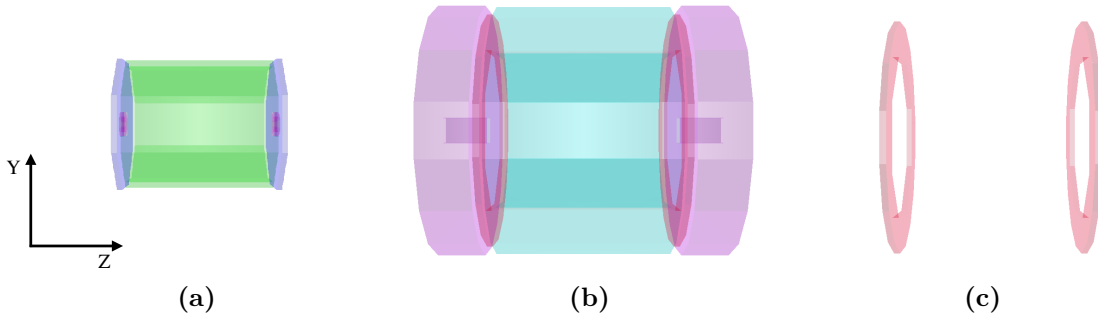


Figure 1.6: A PandoraPFA event display showing the nominal ILD calorimeters. (a) the ECal, (b) the full HCal and (c) the HCal ring, which covers the barrel/endcap cross-over region.

1.2.4 MIP Scale Determination in PandoraPFA

The MIP scale in PandoraPFA is set by simulating 10 GeV μ^- events and creating the distribution of combined calorimeter hit energies. The MIP scale in PandoraPFA must to be determined for the calorimeters and, in contrast to the digitiser, the muon chamber. Consequently, an additional distribution showing the calorimeter hit energy for

the muon chamber must be constructed at this stage of the calibration. As was done for the digitiser, a direction correction factor was applied to the hit energies account for the path length of the MIP through the active medium of the calorimeter and no selection cuts were applied.

Examples of the distributions used to set the MIP scale in PandoraPFA can be found in figure 1.7. Due to the energy thresholds applied in the digitiser, there are fewer populated bins with low hit energies. The double peak structure observed in the ECal calorimeter hit energy distribution is expected given the ECal absorber material thickness doubling in the back 10 layers of the ECal. The MIP peaks used for defining the MIP scale in PandoraPFA, figure 1.7, are broader than those used for determining MIP scale setting in the digitiser, 1.1, as the realistic effects applied by the digitiser are only present in the combined calorimeter hit energy distributions.

1.2.5 Electromagnetic Scale in PandoraPFA

Setting the electromagnetic scale in PandoraPFA is performed by examining the energies of particles reconstructed by PandoraPFA. The reconstruction is performed using the combined calorimeter hit energies that were set by the digitiser and having applied the noise vetoing MIP cuts.

The electromagnetic scale in the ECal, β_{ECal}^{EM} , is determined using simulated photons at $E_{MC} = 10$ GeV. To ensure that the events used for this part of the calibration are largely confined to the ECal, a cut requiring less than 1% of the reconstructed energy to be found outside the ECal is applied. Furthermore, only events reconstructed as a single photon are used to veto conversions. The impact of the selection cuts on the electromagnetic energy measured in the ECal for 10 GeV photons is shown in figure 1.8a. The peak at zero electromagnetic energy in the ECal is due to events traveling down the beam pipe and photon conversions. In photon conversion events, the calorimetric energy deposits made by the e^\pm are associated to charged particle tracks. In this case, the energy measured using the calorimeters will be reported as zero because the charged particle tracks are used to determining the reconstructed particle energies. The tail of events with low electromagnetic energy in the ECal occurs primarily due pattern recognition failures in photon conversion events. In these events a small fraction of the calorimetric energy deposits made by the e^\pm are not associated to charged particle tracks and instead are reconstructed as separate photons with a reconstructed energy much less than E_{MC} .

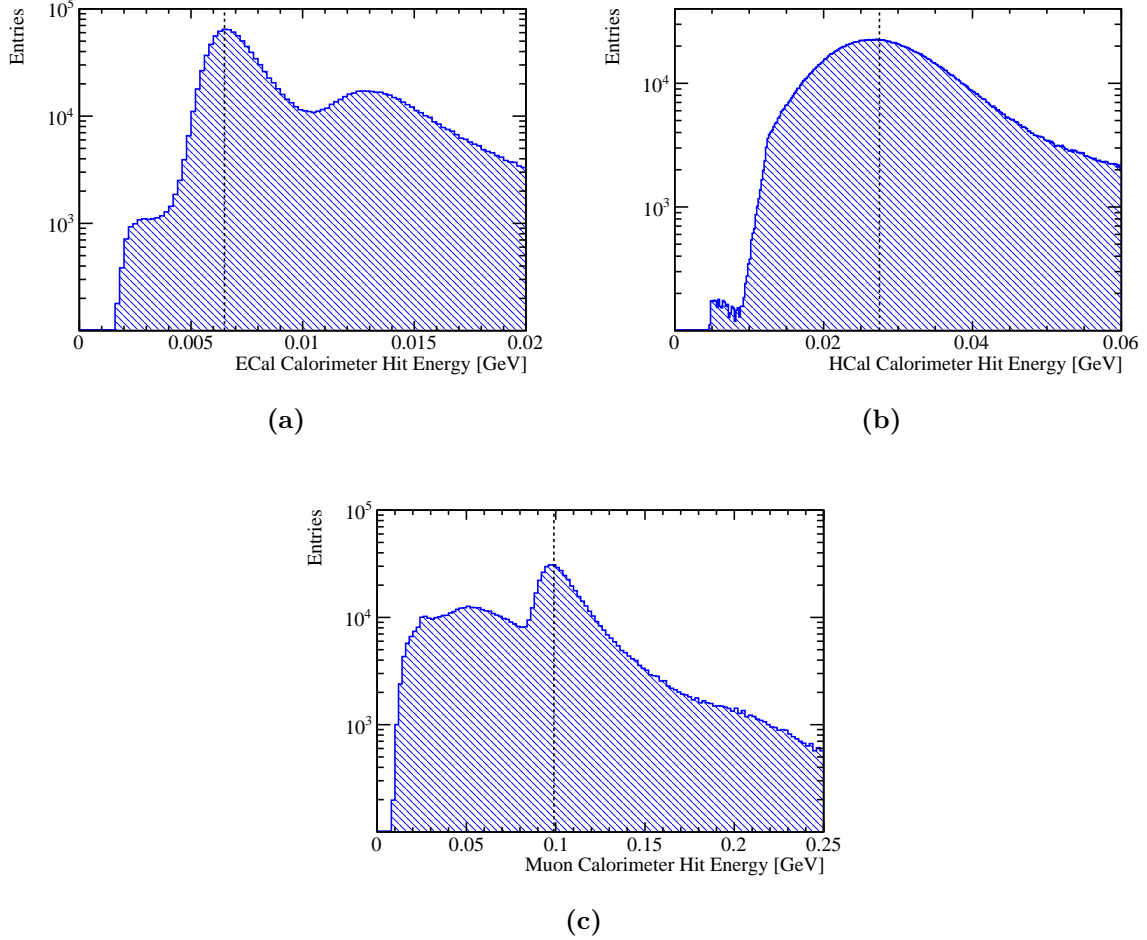


Figure 1.7: The combined calorimeter hit energy distributions for (a) the ECal, (b) the HCal and (c) the muon chamber for 10 GeV μ^- events. These hit energies were corrected to account for the path length of the muons through the active medium of the calorimeter. The vertical black dotted lines indicate the position of the peak in each of these distributions that is used for defining the MIP scale in PandoraPFA.

The fitting procedure follows that used for the ECal digitisation, described in section 1.2.3.1, whereby a trial calibration for the electromagnetic energy scale in the ECal, β_{ECal}^{EM0} , is first assumed. The initial trial calibration is approximate and is iteratively updated until it converges to within a chosen tolerance. Using the trial calibration, the photons are reconstructed and the distribution of the electromagnetic energy in the ECal created. A Gaussian fit is then applied to this distribution in the range with the smallest root mean square containing at least 90 % of the data. The mean of the fitted Gaussian,

E_{Fit} , is then used to scale $\beta_{\text{ECal}}^{EM0}$ in the following way

$$\beta_{\text{ECal}}^{EM0} \rightarrow \beta_{\text{ECal}}^{EM} = \beta_{\text{ECal}}^{EM0} \times \frac{E_{\text{MC}}}{E_{\text{Fit}}} . \quad (1.7)$$

An example distribution and fit used in the calibration of the nominal ILD detector model can be found in figure 1.8b. This procedure is repeated using the updated β_{ECal}^{EM} until E_{Fit} falls within a specified tolerance. The tolerance applied here was $|E_{\text{Fit}} - E_{\text{MC}}| < E_{\text{MC}} \times 0.5\%$. The binning for the fitted histogram is chosen such that the bin width is equal to the desired target tolerance on E_{Fit} , e.g. $E_{\text{MC}} \times 0.5\% = 0.05$ GeV. This tolerance is tighter than was applied for the digitisation as it is these and only these energies that are used in downstream analyses.

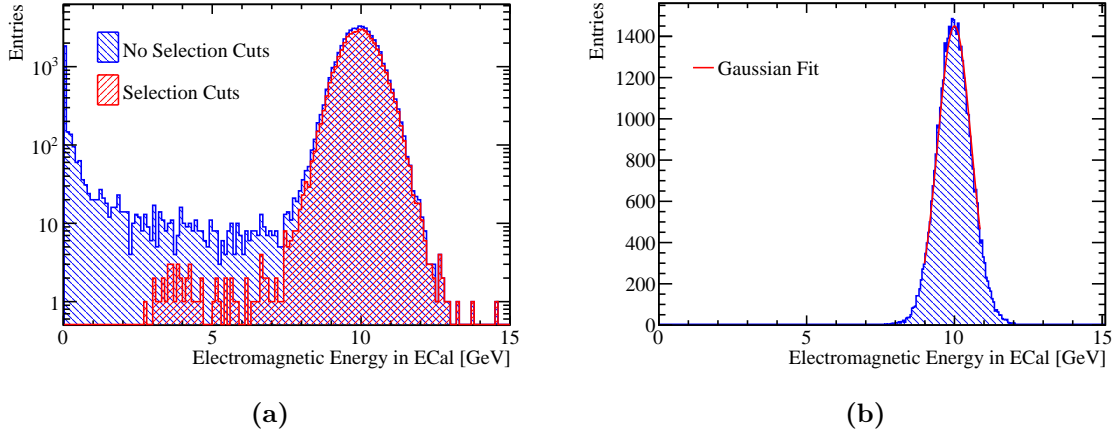


Figure 1.8: (a) The sum of the electromagnetic energy measured in the ECal for simulated 10 GeV photons with and without the selection cuts. (b) Gaussian fit to sum of the electromagnetic energy deposited in the ECal for simulated 10 GeV photons with selection cuts.

1.2.6 Hadronic Scale in PandoraPFA

The hadronic energy scale factors for the ECal, $\beta_{\text{ECal}}^{\text{Had}}$, and HCal, $\beta_{\text{HCal}}^{\text{Had}}$, are determined using simulated K_L^0 events at $E_{\text{MC}} = 20$ GeV. As the ECal contains approximately one nuclear interaction length, a non-negligible amount of hadronic energy will be deposited in the ECal, which makes the hadronic scale in the ECal, $\beta_{\text{ECal}}^{\text{Had}}$, important for detector performance. The hadronic scale in the ECal and HCal are simultaneously set as it is unfeasible to create a large sample of 20 GeV K_L^0 s that are fully contained within the ECal.

For the reasons outlined in section 1.2.3.2, the target reconstructed energy for the sample of K_L^0 used for setting the hadronic energy scale is the kinetic energy, E_K , as opposed to the total energy. To ensure the events used are not affected by leakage of energy out of the back of the HCal, a cut is applied that vetoes events where energy is deposited in the outermost 10% of the HCal. In addition, a cut requiring a single neutral hadron to be reconstructed is applied to veto events with reconstruction failures and decays in the tracker. Finally, it is required that the total hadronic energy measured within the calorimeters falls within three σ of the kinetic energy of the K_L^0 , where σ is taken to be $55\% \times \sqrt{E_K}$ GeV. This definition for σ is approximately the energy resolution for neutral hadrons using the nominal ILD HCal [1]. This cut ensures that when fitting the two dimensional distribution of hadronic energy measured in the ECal and HCal, outliers do not skew the fit. The impact of these selection cuts can be seen in figure 1.9.

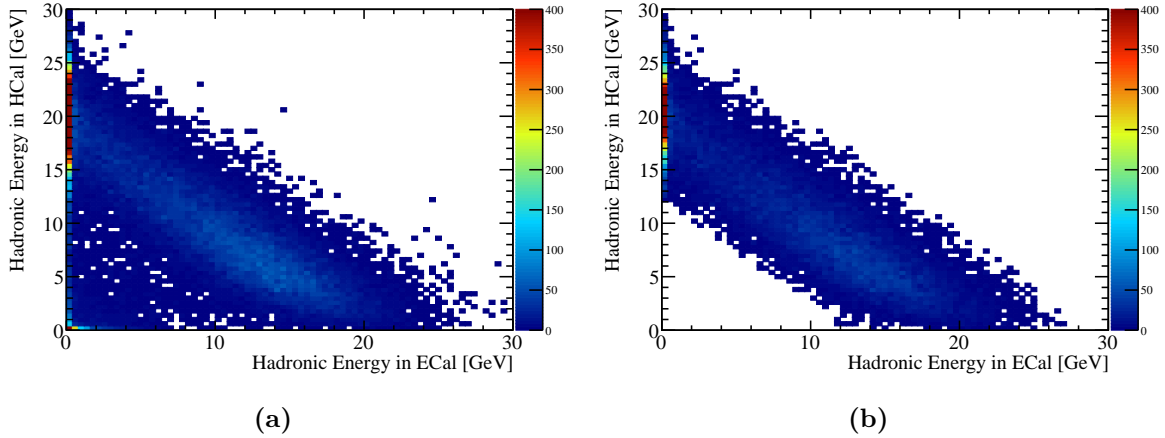


Figure 1.9: The distribution of hadronic energy measured in the ECal and HCal for 20 GeV K_L^0 events (a) without selection cuts and (b) with selection cuts.

Determining the hadronic scale in PandoraPFA is an iterative process and begins by assuming trial values, β_{ECal}^{Had0} and β_{HCal}^{Had0} , for the hadronic scale calibration factors β_{ECal}^{Had} and β_{HCal}^{Had} . The K_L^0 events are first reconstructed using the trial scale factors. Then a linear fit is applied to the two dimensional distribution of the reconstructed hadronic energies measured in the ECal and HCal for events passing the selection cuts. The best fit is obtained by minimising χ^2 with respect to variables describing a linear fit to the distribution. In this case, χ^2 is defined as

$$\chi^2(\delta_{ECal}^{Had}, \delta_{HCal}^{Had}) = \sum_i \left(\frac{r_i}{\sigma_{r_i}} \right)^2, \quad (1.8)$$

where r_i is the perpendicular distance in the two dimensional plane of hadronic energies measured in the ECal and HCal from the point (x_i, y_i) to a straight line passing through the points $(\delta_{ECal}^{Had}, 0)$ and $(0, \delta_{HCal}^{Had})$. In this definition, x_i and y_i are the hadronic energies measured in the ECal and HCal respectively for event i . The variables δ_{ECal}^{Had} and δ_{HCal}^{Had} describe a linear fit to the hadronic energy distribution, which are to be varied when minimising χ^2 . The explicit definition of r_i is given in equation 1.9 and illustrated in figure 1.10. The uncertainty on r_i is given by σ_{r_i} , which is explicitly defined in equation 1.10. This uncertainty is calculated by propagating the uncertainties on x_i and y_i , which are assumed to be $\sigma_{x_i/y_i} = 55\% \times \sqrt{x_i/y_i}$, into the expression for r_i . The sum runs over all events, i , passing the selection cuts.

$$r_i = \frac{y_i \delta_{ECal}^{Had} + x_i \delta_{HCal}^{Had} - \delta_{ECal}^{Had} \delta_{HCal}^{Had}}{\sqrt{(\delta_{ECal}^{Had})^2 + (\delta_{HCal}^{Had})^2}}, \quad (1.9)$$

$$\sigma_i = \frac{(\sigma_{y_i} \delta_{ECal}^{Had})^2 + (\sigma_{x_i} \delta_{HCal}^{Had})^2}{\sqrt{(\delta_{ECal}^{Had})^2 + (\delta_{HCal}^{Had})^2}}. \quad (1.10)$$

The minimisation of χ^2 is done by stepping over a range of δ_{ECal}^{Had} and δ_{HCal}^{Had} centred about

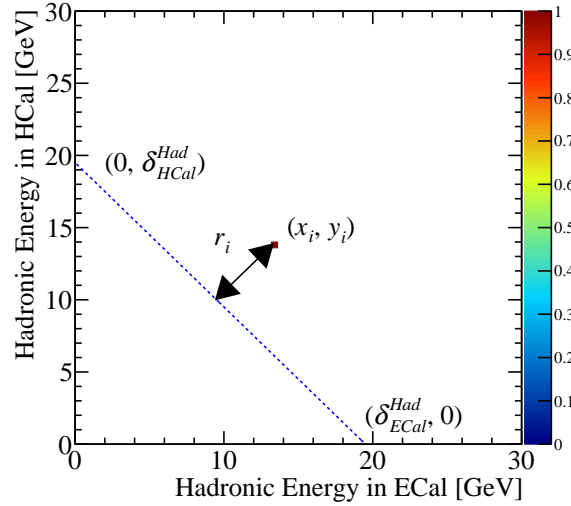


Figure 1.10: An example showing the definition of r_i . The blue dotted line corresponds to $y_i = \delta_{HCal}^{Had} - x_i \delta_{HCal}^{Had} / \delta_{ECal}^{Had}$.

the ideal value of E_K in search for the minimum χ^2 . Once the minima in χ^2 is found the trial calibration factors β_{ECal}^{Had0} and β_{HCal}^{Had0} are rescaled to correct for any deviation from

the desired fit as follows

$$\beta_{ECal}^{Had0} \rightarrow \beta_{ECal}^{Had} = \beta_{ECal}^{Had0} \times \frac{E_K}{\Delta_{ECal}^{Had}} , \quad (1.11)$$

$$\beta_{HCal}^{Had0} \rightarrow \beta_{HCal}^{Had} = \beta_{HCal}^{Had0} \times \frac{E_K}{\Delta_{HCal}^{Had}} , \quad (1.12)$$

where Δ_{ECal}^{Had} and Δ_{HCal}^{Had} are the values of δ_{ECal}^{Had} and δ_{HCal}^{Had} giving the minimum χ^2 . The step size used for minimising χ^2 with respect to δ_{ECal}^{Had} and δ_{HCal}^{Had} was chosen such that a single step would correspond to the final tolerance on δ^{Had} , which in this case is ≈ 0.1 GeV. This procedure is then repeated using the updated hadronic scaling factors until Δ_{ECal}^{Had} and Δ_{HCal}^{Had} both fall within a specified final tolerance, which in this case is taken to be $|\Delta_{E/HCal}^{Had} - E_K| < E_K \times 0.5\% \approx 0.1$ GeV.

The electromagnetic scale in the HCal, β_{HCal}^{EM} , is chosen to be equal to the hadronic scale in the HCal, β_{HCal}^{Had} . For the ILC and CLIC, β_{HCal}^{EM} is not a critical parameter in the reconstruction as photons are largely contained within the ECal meaning little to no electromagnetic energy is measured in the HCal.

Setting the hadronic scale in PandoraPFA ensures that the energy estimators for neutral hadrons are accurate at 20 GeV, however, this is not true for all energies. The undetectable energy component of a hadronic shower varies as a function of particle shower energy [7], which means the response of a calorimeter to neutral hadrons non-linear with the hadron energy. This is an inherent limitation of this calibration procedure that will be addressed by the development of more sophisticated energy estimators in subsequent chapters.

1.2.7 Summary

The procedure for setting the MC response in the linear collider detector simulation has been outlined. This procedure ensures that when modifying the detector simulation, the response of the detector will yield reliable energy estimators for particles showering in the calorimeter. For completion, after this calibration procedure has been applied, retraining of the likelihood data used by specific algorithms in PandoraPFA for the reconstruction of photons can be performed.

1.3 Novel Energy Estimators

This section describes two novel energy estimators that are introduced with a view to improving the energy resolution for hadronic showers. Two techniques will be discussed: HCal hit energy truncation, which focuses on limiting the impact of Landau fluctuations; and software compensation, which focuses on obtaining a compensating calorimeter response. Both of these techniques are implemented by introducing weights, ω^i , to calorimetric energy deposits made by showering particles in the HCal. The energy of a showering particle, $E_{Cluster}$, is determined by grouping together a clusters of calorimeter hits and summing their energies. When weights are applied to HCal hits this energy estimator becomes

$$E_{Cluster} = \sum_{ECal\ hits, i} E_{ECal}^i + \sum_{HCal\ hits, i} E_{HCal}^i \omega^i(\rho^i) . \quad (1.13)$$

Weights are only applied to calorimeter hits in the HCal as these techniques modify the energy of hadronic showers, which are primarily contained within the HCal. The weights, ω^i , vary a function of the energy density of the calorimeter hit, $\rho^i = E_{HCal}^i/V$ where V is the physical volume of a calorimeter hit in the HCal, which includes the both the active and absorber layer thicknesses.

Although the exact weights depend on the implementation of the technique, a general feature is that at large E_{HCal}^i the weight is less than one. This limits the impact of spuriously high energy hits caused by Landau fluctuations. The energy loss probability distribution function for scintillator detectors, such as the ILD HCal, is given by a Landau function [8]. Energy deposits from the high energy tail of this distribution, which are known as Landau fluctuations, account for high energy knock-on electrons that appear within particle showers [9]. As Landau fluctuations deposit a disproportionately large amount of energy with respect to the bulk of the particle shower, they can lead to overestimates of the particle shower energy.

The energy loss probability distribution function for n particles passing through a calorimeter hit is given by the convolution of n Landau functions, which by the central limits theorem will tend to a Gaussian as n becomes large. Consequently, as the average number of particles passing through a calorimeter hit increases, the high energy tail in the energy loss probability distribution function for the hit becomes less pronounced and the impact of Landau fluctuations decreases. This means that the impact of Landau fluctuations on energy measurements is dictated by the density of a particles within a

particle shower and the transverse segmentation, or cell size, of the calorimeter in use. If the transverse segmentation, or cell size, of a calorimeter decreases, the average number of particles passing through each hit decreases and the impact of Landau fluctuations increases. Any technique used for minimising the impact of Landau fluctuations will be sensitive to the transverse segmentation of the calorimeters in use.

1.3.1 HCal Hit Energy Truncation

The first technique to be examined is a simple truncation of the hadronic energy, E , recorded in any given HCal hit

$$E \rightarrow E' = \begin{cases} E & \text{if } E < \kappa , \\ \kappa & \text{otherwise ,} \end{cases} \quad (1.14)$$

where κ is the value of the truncation. This improves the energy estimators for hadronic clusters by limiting the impact of Landau fluctuations. In terms of ω introduced in equation 1.13 the truncation corresponds to

$$\omega(\rho) = \begin{cases} 1 & \text{if } \rho \times V < \kappa , \\ \frac{\kappa}{\rho \times V} & \text{otherwise .} \end{cases} \quad (1.15)$$

This weight as a function of hit energy density is shown in figure 1.11.

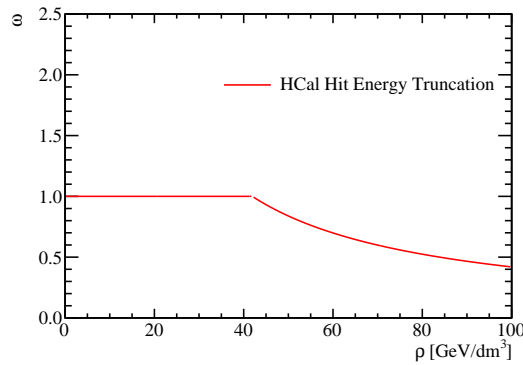


Figure 1.11: The weights, ω , used in the HCal hit energy truncation as a function of the energy density of the HCal hit, ρ . The truncation shown here corresponds to a 1 GeV truncation in the nominal ILD HCal.

1.3.1.1 Legacy Energy Corrections

Alongside the HCal hit energy truncation, PandoraPFA also applied two other energy corrections designed at limiting the impact of Landau fluctuations. They are:

- **Clean Clusters.** This algorithm checks to see whether the energy measured within a calorimeter hit is anomalously high. Anomalously high energy hits are defined as hits where the energy contained within the hit is greater than 10% of the energy of the cluster that the hit has been associated to. If a hit is deemed to have an anomalously high energy and if this energy is above a threshold (0.5 GeV) the hit energy used by PandoraPFA is modified. The updated hit energy is taken as the average hit energy in the calorimeter layers immediately before and after the layer containing the high energy hit.
- **Scale Hot Hadrons.** This algorithm calculates the average energy of the calorimeter hits in a given cluster in units of, normally incident, MIP equivalent particles. If this number is larger than a certain value, default 15 MIPs per hit, the cluster energy is rescaled to give a lower average number of MIPs per hit, default is 5 MIPs per hit.

In the reconstruction, these corrections are applied to each cluster of calorimeter hits, irrespective of the location of that cluster in the detector. These algorithms, with the HCal hit truncation, form the "legacy" energy corrections that are used by PandoraPFA when performing the event reconstruction.

1.3.1.2 Impact on Single Particle Energy Resolution

Figure 1.12a shows the energy resolution for neutral hadrons as a function of the HCal hit energy truncation. The optimal truncation for the ILD detector model simulation was 1 GeV and, using this truncation, a neutral hadron energy resolution of $\sim 8.8\% = 62\%/\sqrt{E(\text{GeV})}$ was obtained for $E = 50 \text{ GeV } K_L^0$ events. In comparison, the neutral hadron energy resolution for $E = 50 \text{ GeV } K_L^0$ events obtained without a truncation was $\sim 10.4\% = 74\%/\sqrt{E(\text{GeV})}$. Smaller energy truncations begin to truncate the energy of calorimeter hits produced in typical hadronic shower development, while larger truncations allow for a larger impact from Landau fluctuations. Both of these effects result in worsening neutral hadron energy resolutions. For completeness the photon energy resolutions as a function of HCal hit energy truncation are shown in figure 1.12b.

As expected the photon energy resolution is unaffected by the HCal hit energy truncation as the photons are largely contained within the ECal.

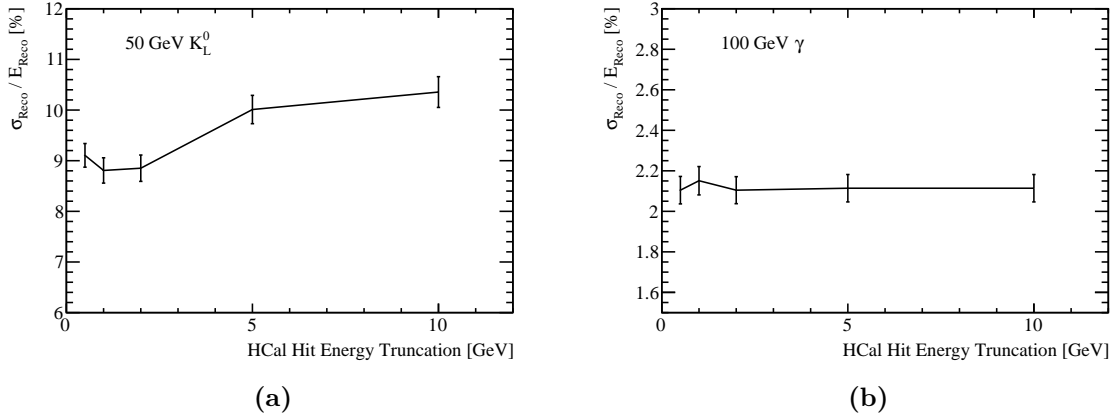


Figure 1.12: The energy resolution as a function of HCal cell truncation for (a) 50 GeV K_L^0 events and (b) 100 GeV photons using the nominal ILD detector model.

1.3.1.3 Impact on Jet Energy Resolution

Figure 1.13 shows the jet energy resolution as a function of jet energy for selected values of the HCal hit energy truncation. The trends in this plot are complex as the optimal HCal hit energy truncation varies with the jet energy. For 45.5 GeV jets, the best jet energy resolution, $\sim 3.6\%$, is obtained using a 0.5 GeV truncation, while for 180 GeV jets, the best jet energy resolution, $\sim 2.9\%$, is obtained using a 1 GeV truncation. This is expected because at low jet energies the average number of particles passing through each active calorimeter hit will be small, meaning the impact of Landau fluctuations is large and that to limit them a low truncation energy is needed. As the jet energy increases more particles on average pass through each calorimeter hit and the impact of Landau fluctuations decreases.

It is clear that a 1 GeV HCal hit energy truncation is beneficial for the performance of the nominal ILD detector model since the jet energy resolution is reduced by roughly $\sim 0.15\%$ across the jet energy range from 45.5 GeV to 250 GeV. As the HCal hit truncation technique offers significant performance gains, it is used for the calorimeter optimisation studies presented in chapter 2. These studies include optimisation of the HCal cell size. Increasing the HCal cell size will increase the average number of particles passing through each calorimeter hit, which in turn reduces the impact of Landau fluctuations and vice

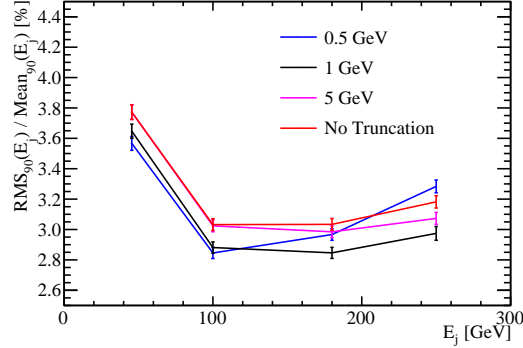


Figure 1.13: The jet energy resolution as a function of jet energy for various HCal hit energy truncations. The results shown use the nominal ILD detector model, which contains $30 \times 30 \text{ mm}^2$ square scintillator tiles in the HCal.

verse. For all detector models considered where the HCal cell size was varied, the HCal hit energy truncation was reoptimised to account for the changing impact of Landau fluctuations. For detector models with a HCal cell size of $10 \times 10 \text{ mm}^2$, $20 \times 20 \text{ mm}^2$, $30 \times 30 \text{ mm}^2$, $40 \times 40 \text{ mm}^2$, $50 \times 50 \text{ mm}^2$ and $100 \times 100 \text{ mm}^2$ the reoptimised truncation values were 0.5, 0.75, 1, 1.5, 2 and 5 GeV respectively. Furthermore, the average particle density in a HCal hit will also be sensitive to the properties of the absorber material used in the calorimeters, therefore, the HCal hit energy truncation was also reoptimised in the HCal absorber material study. The optimal truncation energy cut for the $30 \times 30 \text{ mm}^2$ cell size tungsten HCal option was 5 GeV, while for all other detector models considered it was 1 GeV. The cause of increased truncation energy cut for tungsten is discussed in section 2.3.5.

Understanding the affect of the HCal hit energy truncation is crucial when performing optimisation studies. This can be seen in figure 1.14, which shows the results of the HCal cell size optimisation study when using a 1 GeV truncation and when optimising the truncation for each detector model. By applying a uniform HCal hit energy truncation the importance of the HCal cell size to particle flow calorimetry is vastly overinflated. For example, if the HCal cell size is increased from 10 mm to 100 mm the jet energy resolution for 250 GeV jets goes from $\sim 2.8\%$ to $\sim 4.5\%$ for the flat 1 GeV truncation, but only $\sim 3.5\%$ when using an optimised truncation. As the jet energy and HCal cell size increase, the flat 1 GeV truncation throws away a larger fraction of typical hadronic shower energy measurements, which causes the jet energy resolution to degrade rapidly.

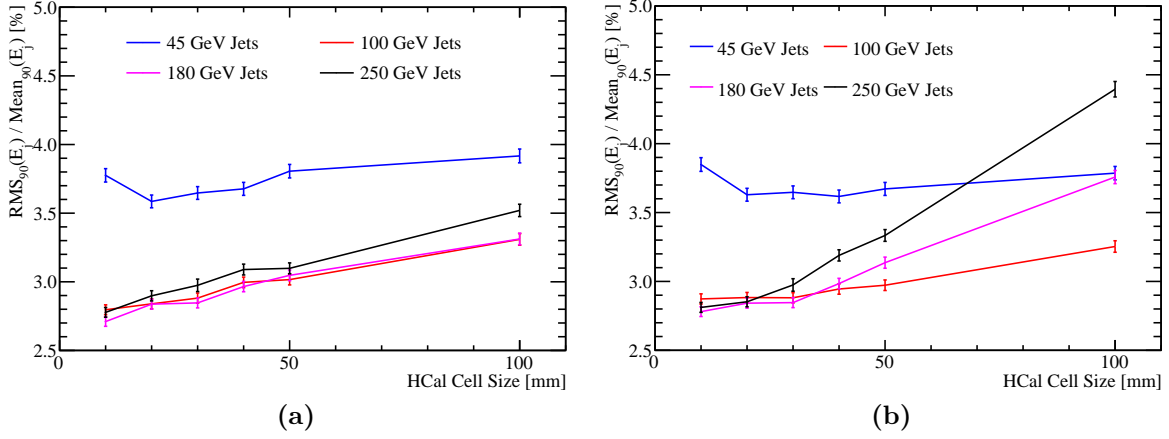


Figure 1.14: The jet energy resolution as a function of HCal cell size in the ILD detector model using a HCal hit energy truncation that is (a) optimised and (b) fixed at 1 GeV.

1.3.2 Software Compensation

Particle showers that are produced when a hadron interacts with a calorimeter contain two components [7]; an electromagnetic shower core, which originates from the production and decay of π^0 s and η s, and a hadronic shower component originating from other interacting and decaying particles. By identifying each of these components in the reconstruction, it is possible to modify their energies to give a compensating calorimeter response. This technique known as software compensation.

Software compensation achieves a compensating calorimeter response by applying weights, as introduced in equation 1.13, that modify the energy of calorimeter hits in the HCal. These weights increase the energy found in the hadronic hits to compensate for the undetectable energy component found in hadronic showers. Additionally, these weights reduce the energy of spuriously high energy hits to minimise the impact of Landau fluctuations. The weights vary as a function of the calorimeter hit energy density, ρ^i , and the uncompensated energy of the particle shower, E_{Raw} , where

$$E_{Raw} = \sum_{ECal \text{ hits}, i} E_{ECal}^i + \sum_{HCal \text{ hits}, i} E_{HCal}^i. \quad (1.16)$$

The electromagnetic and hadronic components of a hadronic particle shower are treated differently in this approach by applying weights that are sensitive to the energy density of the calorimeter hits. Hits with large energy densities are likely to be part of the electromagnetic core, while low energy density hits are likely to be part of satellite

hadronic hits around the electromagnetic shower core [11]. By tailoring the weights as a function of the energy density, a compensating calorimeter response can be obtained. Figure 1.15 shows the electromagnetic and hadronic shower components, determined by the energy density of the calorimeter hits, for a hadronic shower in a 500 GeV $Z \rightarrow uds$ di-jet event.

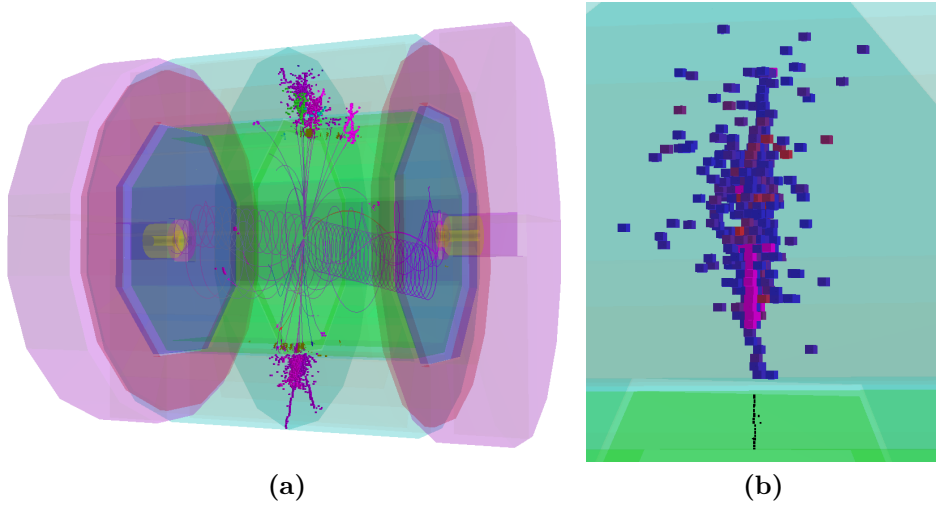


Figure 1.15: An event display for a 500 GeV $Z \rightarrow uds$ di-jet event reconstructed using the nominal ILD detector. (a) The full event environment. (b) A single hadronic cluster from the same event where shading indicates the energy density in the HCal. High energy density cells are coloured red, while lower energy density cells are coloured blue. All ECal hits are shaded black. The high energy density electromagnetic core of the selected hadronic cluster is clearly visible.

The software compensation weights also depend on E_{Raw} , the total raw cluster energy, to account for the sensitivity of the hit energy density distribution on the total particle shower energy. For hadronic showers, the fraction of the total energy carried in the electromagnetic core increases as the total shower energy increases [7], therefore a dependency of the weights on E_{Raw} is needed to obtain a compensating calorimeter response across a wide range of energies.

The precise form of the weights used in this technique are [11]

$$\omega(E_{Raw}, \rho) = p_1(E_{Raw}) \times \exp(p_2(E_{Raw}) \times \rho) + p_3(E_{Raw}) , \quad (1.17)$$

$$(1.18)$$

with

$$p_1(E_{Raw}) = p_{11} + p_{12} \times E_{Raw} + p_{13} \times E_{Raw}^2 \quad (1.19)$$

$$p_2(E_{Raw}) = p_{21} + p_{22} \times E_{Raw} + p_{23} \times E_{Raw}^2 \quad (1.20)$$

$$p_3(E_{Raw}) = \frac{p_{31}}{p_{32} + \exp(p_{33} \times E_{Raw})} , \quad (1.21)$$

where $p_{\alpha\beta}$ are constants and

$$E_{Raw} = \sum_{ECal \text{ hits}, i} E_{ECal}^i + \sum_{HCal \text{ hits}, i} E_{HCal}^i . \quad (1.22)$$

The parameters $p_{\alpha\beta}$ were determined by minimising $\chi^2(p_{\alpha\beta})$ where

$$\chi^2(p_{\alpha\beta}) = \sum_{Events} \left(\frac{(E_{Cluster}^{SC}(p_{\alpha\beta}) - E_{MC})}{0.5 \times \sqrt{E_{MC}}} \right)^2 \quad (1.23)$$

where the sum runs over single K_L^0 events that ranged in energy from 10 to 100 GeV in steps of 10 GeV. At each energy the same number of events was used to avoid biasing to particular energies. In each event, $E_{Cluster}^{SC}$ is the software compensated energy estimator for the reconstructed event and E_{MC} is the MC energy of the K_L^0 . Normalising the deviation of $E_{Cluster}^{SC}$ from E_{MC} by the stochastic term in the HCal energy resolution, $\sim 50\% \times \sqrt{E}$, made sure events of different MC energy contributed the same weight to χ^2 .

Figure 1.17 shows ω as a function of ρ for selected values of E_{Raw} and figure 1.16 shows p_1 , p_2 and p_3 as a function of E_{Raw} . These weights shown in figures 1.17 and 1.16 were obtained by training the software compensation technique on samples simulated using the nominal ILD detector model. Figure 1.17 shows that the high energy density hits are being reduced in energy to compensate for the effects of Landau fluctuations, while the low energy density hits are being increased in weight to compensate for the undetectable energy component found in hadronic showers. Furthermore, the weights vary as a function of the raw hadronic shower energy to account for the changing energy density topology of hadronic showers with increasing shower energy.

The software compensation technique is applied in the PandoraPFA framework in the form of an energy correction function, which means whenever the energy of a cluster of hits is considered by PandoraPFA the software compensated energy is used. Applying software compensation in this way benefits the detector energy resolution in two ways;

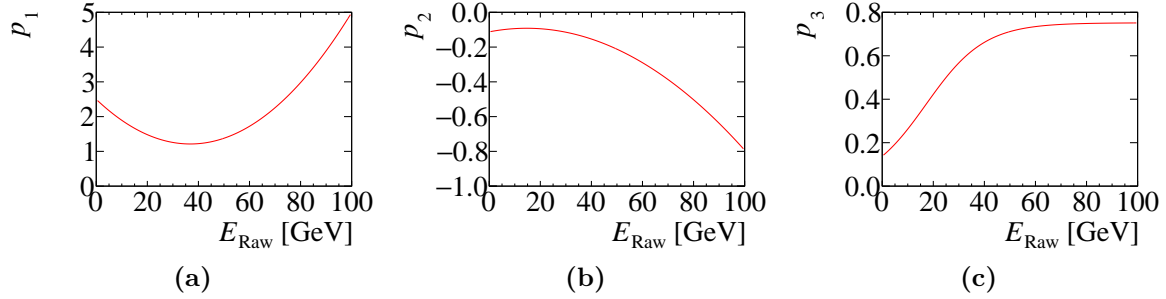


Figure 1.16: The software compensation parameters (a) p_1 , (b) p_2 and (c) p_3 as a function of E_{Raw} , the total raw cluster energy. These weights were obtained by training the software compensation technique on samples simulated using the nominal ILD detector model.

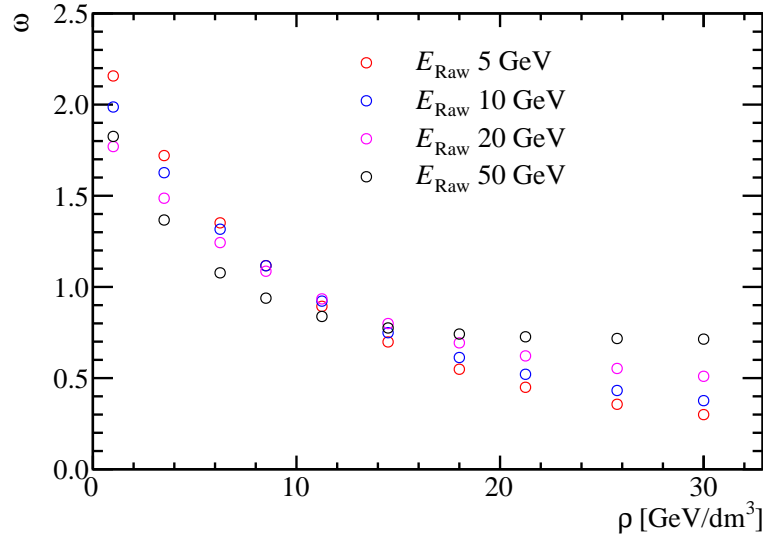


Figure 1.17: The software compensation weight applied to a calorimeter hit as a function of calorimeter hit energy density for various cluster energies.

firstly, the intrinsic energy resolution of the detector improves and secondly, the confusion contribution to the energy resolution is reduced.

As software compensation only modifies the energy of HCal hits there is freedom to apply further energy corrections to the ECal hits. Applying the "Clean Clusters" logic, described in section 1.3.1.1, to the ECal hits alongside software compensation was found to be beneficial to the jet energy resolution. Therefore, the application of software compensation within PandoraPFA implicitly involves the application of the "Clean Clusters" logic to the ECal hits.

Software compensation was tuned using a maximum K_L^0 energy of 100 GeV, therefore, it is only applied to clusters where $E_{Raw} < 100$ GeV; sensible behaviour outside this range cannot be ensured. While it would be possible to modify the energy range of the training sample to go to higher energies, hadronic clusters with energy greater than 100 GeV will be rare at the ILC-like energies, i.e. $\sqrt{s} \leq 500$ GeV, considered here.

1.3.2.1 Impact on Single Particle Energy Resolution

Figure 1.18 shows the energy resolution as a function of MC energy for single K_L^0 events obtained using the various energy correction configurations in PandoraPFA. When comparing the energy resolution given by software compensation to that obtained using no energy corrections, it can be seen that software compensation offers an improvement in the energy resolution of $\sim 15\%$ across the energy range considered. The uniformity of this improvement is encouraging, indicating that software compensation is achieving a compensating calorimeter response across this wide range of energies.

Comparing the performance of software compensation to the legacy corrections, described in section 1.3.1.1, it can be seen that software compensation gives a better energy resolution across almost the entire range of energies considered. The only exception to this is around $E_{K_L^0} \sim 50$ GeV where the performance of software compensation and the legacy corrections are comparable. By removing the hit truncation from the legacy options it is clear that the changes in energy resolution when using the legacy options are being driven by the hit truncation. This makes the trend in energy resolution observed using the legacy corrections clear as, at low K_L^0 energies, very few hits are affected by the truncation so the performance is comparable to not using any energy corrections. At high K_L^0 energies, the truncation is too aggressive and removes energy from hits that are not spuriously high leading to a worsening energy resolution. Between these two extremes, $E_{K_L^0} \sim 50$ GeV, the truncation works ideally and the improvement in energy resolution when using the legacy corrections is the largest.

1.3.2.2 Impact on Jet Energy Resolution

The improvements in the intrinsic energy resolution of the detector observed when using software compensation will propagate into the reconstruction of jets. Figure 1.19 shows the jet energy resolution as a function of jet energy when using selected energy correction configurations in PandoraPFA. It can be seen that software compensation improves the

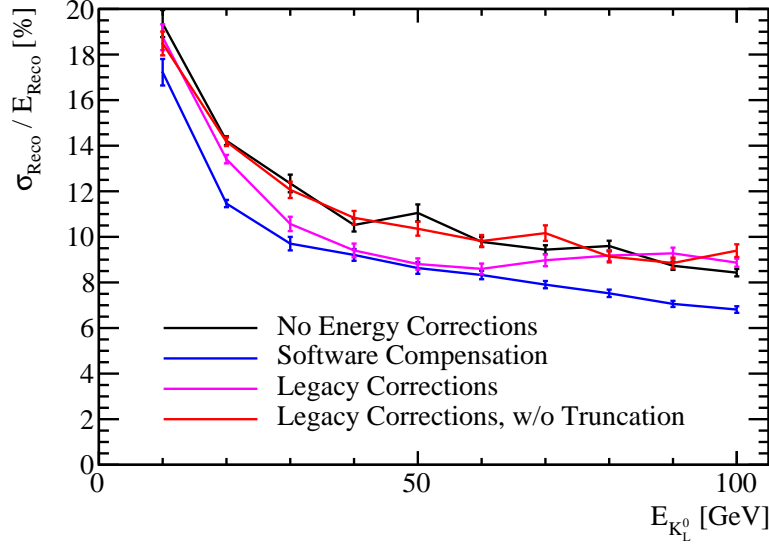


Figure 1.18: The energy resolution as a function of the MC energy for single K_L^0 events using various energy correction settings. The black line represents no energy corrections, the blue line represents software compensation, the magenta line represents the legacy energy corrections and the red line represents the legacy corrections without the HCal hit energy truncation. The nominal ILD detector model was used in these simulations.

jet energy resolution by $\sim 15\%$ across the energy range considered in comparison to using no energy corrections. Furthermore, software compensation offers an improvement in the jet energy resolution of the order of 5% for jet energies $\gtrsim 100$ GeV in comparison to the legacy corrections, which prior to the development of software compensation had given the best jet energy resolutions.

Figure 1.20 shows the intrinsic energy resolution and confusion contributions to the jet energy resolution as a function of jet energy when using selected energy correction configurations in PandoraPFA. The intrinsic energy resolution contribution shows that software compensation is significantly better than all other energy corrections options, which is to be expected from the energy resolution studies presented in section 1.3.2.1. When compared to the legacy energy corrections, software compensation improves the intrinsic energy resolution by up to 12% across the energy range considered, with the largest improvement occurring for 100 GeV jets. As jets contain a broad spectrum of hadronic cluster energies, there is no jet energy for which the intrinsic energy resolution of the detector is comparable between the legacy corrections and software compensation. The confusion contributions to the jet energy resolution when using software compensation

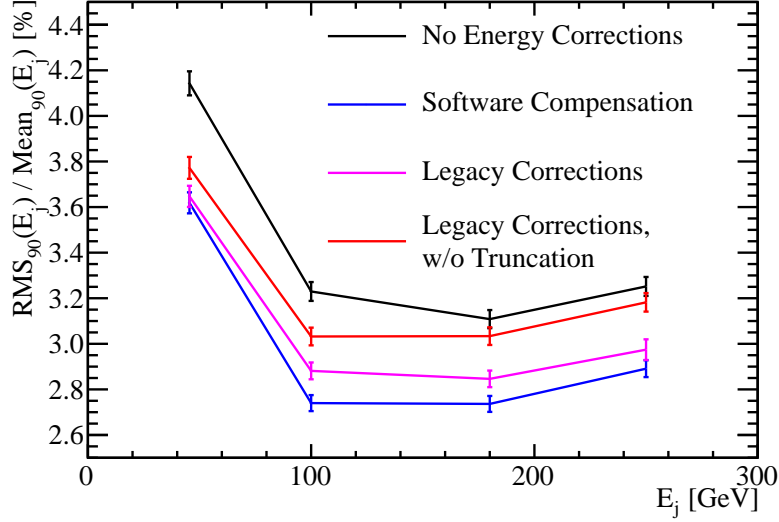


Figure 1.19: The jet energy resolution as a function of the jet energy for a variety of different energy correction options. The black line represents no energy corrections, the blue line represents software compensation, the magenta line represents the legacy energy corrections and the red line represents the legacy corrections without the HCal hit energy truncation. The nominal ILD detector model was used in these simulations.

and the legacy corrections are almost identical. This indicates that the improvement seen in the jet energy resolution when comparing software compensation to the legacy corrections, shown in figure 1.19, is being driven by the intrinsic energy resolution.

The "Clean Clusters" and "Scale Hot Hadrons" energy corrections, i.e. the legacy corrections without the HCal hit energy truncation, benefits the pattern recognition by reducing the confusion contribution. The confusion contribution is reduced by $\sim 18\%$ for 45.5 GeV jets using these energy corrections, however, as the jet energy increases the magnitude of this improvement decreases, such that at 250 GeV jets no improvement is seen. These corrections do not significantly affect the intrinsic energy resolution of the detector. As these corrections benefit pattern recognition, selected aspects of their logic is applied to ECal hits in the software compensation energy correction as previously discussed.

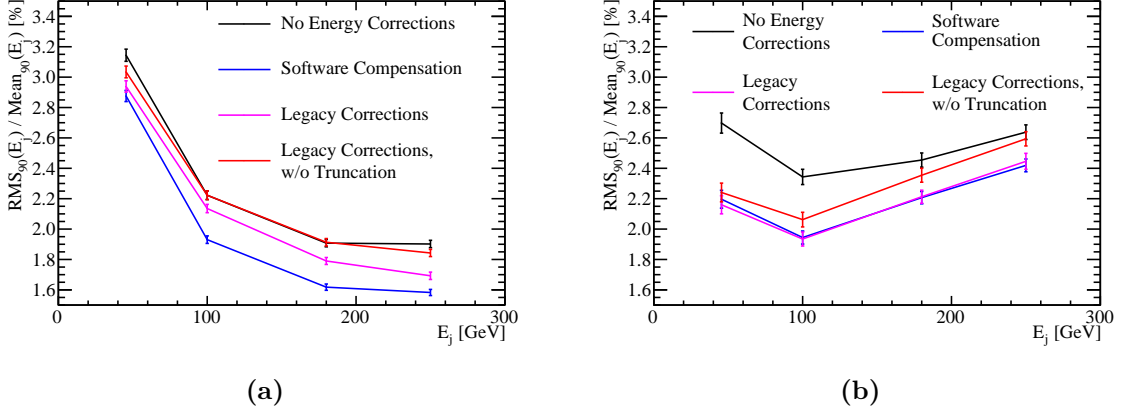


Figure 1.20: The contributions to the jet energy resolution as a function of the jet energy for a variety of different energy correction options. The jet energy resolution contributions presented are (a) the intrinsic energy resolution of the detector and (b) the total confusion contribution. The jet energy resolution obtained using the standard reconstruction is given by the quadrature sum of the intrinsic energy resolution and total confusion contributions. The black line represents no energy corrections, the blue line represents software compensation, the magenta line represents the legacy energy corrections and the red line represents the legacy corrections without the HCal hit energy truncation. The nominal ILD detector model was used in these simulations.

1.3.3 Summary

The effect on both single particle and jet energy resolution of the HCal hit energy truncation and software compensation have been examined. Although relatively simplistic, the HCal hit energy truncation was found to be beneficial for detector performance by limiting the impact of Landau fluctuations. The more sophisticated software compensation procedure was found to be highly effective at producing a compensating calorimeter response across a wide range of energies, which translated into excellent performance in terms of jet energy resolution.

1.4 Timing Cuts

The linear collider will operate using trigger-less readout whereby the recorded data for each sub-detector is read out between collisions of the e^+ and e^- bunches. The bunch train structure for ILC and CLIC is compared in table 1.1. Event selection will proceed through the application of a software trigger. This involves the identification of any

hard interactions, prior to full event reconstruction, and only putting data into the event reconstruction if it is measured within a chosen time window about these interactions. The recorded time of a calorimeter hit, which is cut on to make the time window for the software trigger, is corrected for straight time-of-flight to the IP. This ensures that the amount of time particle showers have to develop in the calorimeters is independent of their position in the detector. The energy resolution of a calorimeter is sensitive to the choice of time window applied because energy measurements made outside the time window are rejected. Therefore, the overall detector performance will be sensitive to the choice of time window used.

At CLIC, the application of a software trigger is challenging because of the 0.5 ns bunch separation. The small bunch separation means the integration time of the calorimeters will span many bunch crossings. When this is combined with the intense beam-induced backgrounds, identification of energy deposits produced from a hard interaction of interest becomes difficult. By placing tight timing constraints on the energy deposits made in the CLIC calorimeters, it is possible to minimise the impact of the beam-induced backgrounds. As well as minimising the impact of the backgrounds, these tight timing requirements will also change how particle showers from the hard interaction of interest are sampled. Understanding the impact of these timing requirements on physics performance is vital to the success of the CLIC experiment. Application of the software trigger at the ILC is less challenging than at CLIC because the bunch separation is much larger, meaning the calorimeters could be read out between bunches, and the beam-induced backgrounds are much smaller.

	ILC 500 GeV	CLIC 3 TeV
Electrons per bunch [10^{10}]	2.0	0.37
Bunches per train	2820	312
Train repetition rate [Hz]	5	50
Bunch separation [ns]	308	0.5

Table 1.1: The train structure for 500 GeV ILC and 3 TeV CLIC [1, 2].

For all choices of time window considered in this study the calibration procedure described in section 1.2 was reapplied. This ensures that the *mean* of the reconstructed energy distributions will not depend on changes in the calorimeter timing window because the calibration will compensate for any energy losses incurred by rejecting energy measurements made outside the time window.

For the results presented in this chapter and the optimisation studies found in chapter 2, a 100 ns timing window was applied to all detector models considered. This value was chosen as it reflects particle shower development time [2] and could be reasonably achieved using readout technology options presently available [12].

1.4.1 Impact on Single Particle Energy Resolution

Figure 1.21 shows the energy resolution of the nominal ILD detector for 100 GeV photons and 50 GeV K_L^0 s as a function of the timing window applied to the calorimeter hits. The timing cut makes little difference to the energy resolution of photons, however, the energy resolution for neutral hadrons gets significantly worse as the time window is reduced. The neutral hadron energy resolution becomes worse by almost 20 % when the time window is reduced from 10^6 ns to 10 ns. These trends are to be expected because electromagnetic showers develop far more rapidly than their hadronic counterparts [7]. This can be seen from figure 1.22, which shows the distribution of the measurement time of calorimeter hits, corrected for time-of-flight, for selected shower components for 91 GeV $Z \rightarrow uds$ events. Hadronic showers develop more slowly as they often involve intermediate states that must decay to continue the propagation of the shower.

If a narrow calorimeter timing window is used, energy measurements from the hadronic shower will be lost and the energy resolution will degrade, which is what is observed. On the other hand, electromagnetic showers develop so rapidly that even the 10 ns time window does not reject many energy measurements.

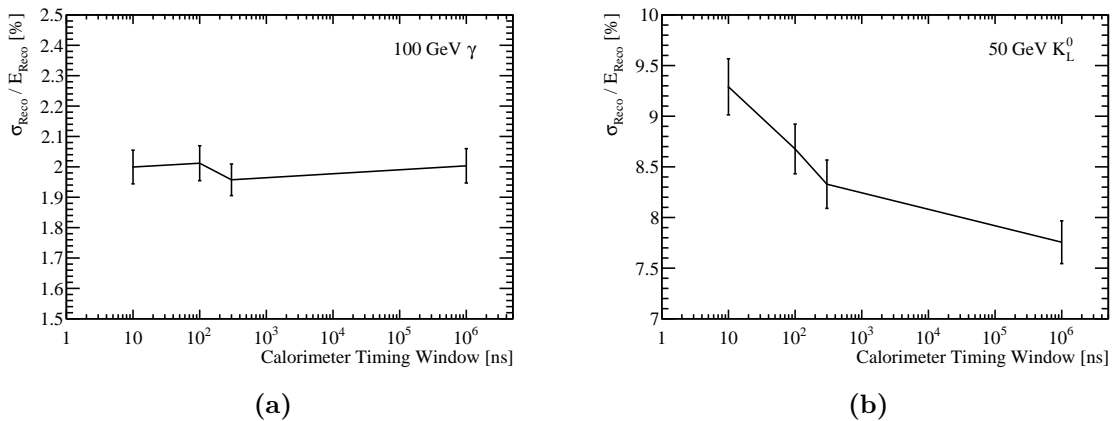


Figure 1.21: The energy resolution as a function of calorimeter timing window for (a) 100 GeV photons and (b) 50 GeV K_L^0 events using the nominal ILD detector model.

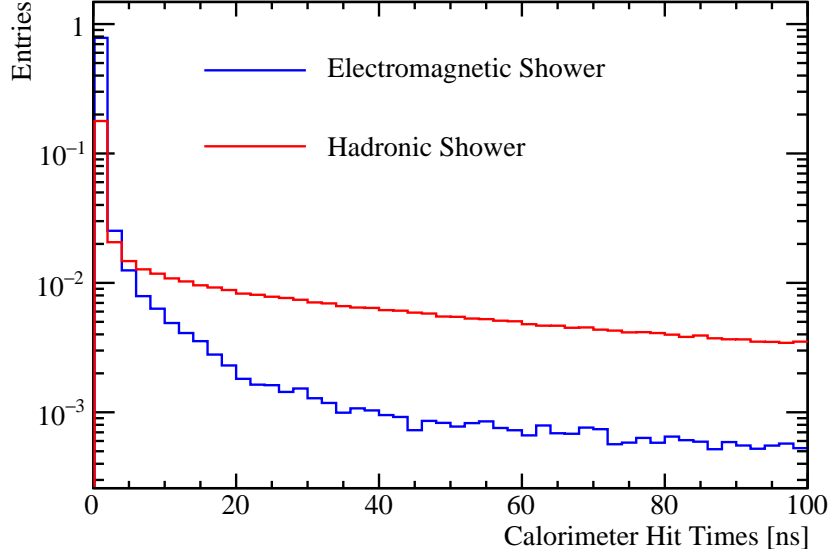


Figure 1.22: The normalised distribution of the time of the electromagnetic and hadronic shower calorimeter hits, corrected for time of flight to the impact point, for 91 GeV $Z \rightarrow uds$ events. Electromagnetic shower energy deposits are deposited very rapidly, while hadronic shower energy deposits are deposited over a much longer time period.

1.4.2 Impact on Jet Energy Resolution

Figure 1.23 shows the jet energy resolution as a function of the jet energy for selected calorimeter time windows. As expected, the jet energy resolution becomes worse when the calorimeter timing window is reduced.

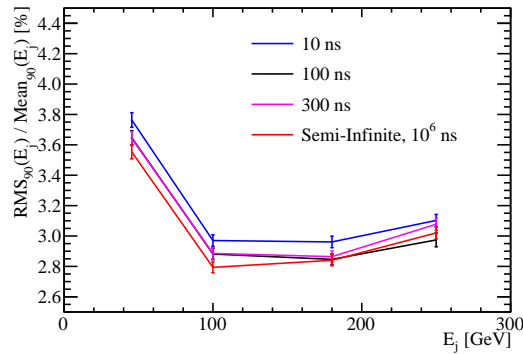


Figure 1.23: The jet energy resolution as a function of jet energy for various calorimeter timing cuts. The nominal ILD detector model was used in these simulations.

The time window applied to the calorimeter hits affects both the neutral hadron and jet energy resolutions with a larger timing window leading to better resolutions. It can be seen that by applying an aggressive choice of time window, such as 10 ns, the jet energy resolution would be degraded because many of the hadronic showers are not fully sampled. However, even using a 10 ns timing cut the jet energy resolutions are still sufficiently low to give excellent detector performance. Both the single particle and jet energy resolutions indicate that the majority of hadronic showers at the energies considered will be fully sampled using a 100 ns time window and that there is little to be gained by increasing this time window further.

1.4.3 Summary

Simulations were performed to study the impact of the calorimeter hit time window used in the software trigger at the linear collider experiments. The energy resolution for electromagnetic showers did not change significantly when varying the size of time window, however, the neutral hadron energy resolution becomes worse as the size of the time window is reduced. The jet energy resolution is also sensitive to the size of the time window used, however, the trend was far weaker than that seen for neutral hadrons because only 10% of the jet energy is carried in the form of neutral hadrons. Increasing the time window beyond 100 ns did not have any significant benefit indicating that the majority of hadronic shows are fully sampled in this time.

Chapter 2

Calorimeter Optimisation Studies

“The simple believes everything, but the prudent gives thought to his steps.”

— Proverbs 14:15

2.1 Introduction

This chapter describes the optimisation of the calorimeters used at the linear collider, with focus placed on obtaining the best energy resolution for jets. Parameters such as the number of layers, cell size and material choices for the calorimeters are investigated. Several global detector parameters such as the magnetic field strength and the inner radius of the ECal are also studied. These parameters are not calorimeter specific, but affect the jet energy resolution obtained from particle flow.

2.2 Electromagnetic Calorimeter Optimisation

The purpose of an electromagnetic calorimeter (ECal) is to measure the energy deposits from electromagnetic showers. The nominal ILD ECal, summarised in table 2.1, is a silicon-tungsten sampling calorimeter. It contains 29 readout layers and 24 radiation lengths (X_0), which is sufficient to contain all but the highest energy electromagnetic showers. The absorber thickness of the last nine layers is twice that of the first 20 layers to reduce the number of readout channels and cost of the calorimeter. The high

longitudinal sampling frequency is crucial for the pattern recognition aspect of particle flow calorimetry, especially in the region where particle showers start developing.

Parameter	Default Value
Cell Size	$5 \times 5 \text{ mm}^2$ square cells
Number of Layers	29 readout layers
Active Material Choice	Silicon or Scintillator
Active Material Thickness	0.5 mm (Silicon) or 2 mm (Scintillator)
Absorber Material Choice	Tungsten
Absorber Material Thickness	20 layers of 2.1 mm followed by 9 layers of 4.2 mm

Table 2.1: The configuration of the silicon and scintillator ECal options for the ILD detector model [1].

The calorimeter performance was simulated for a number of detector models where the following detector parameters were varied:

- Cell size: This is a vital aspect of the detector in the particle flow paradigm as smaller cell sizes leads to better separation between nearby showering particles, which helps to minimise the effect of confusion. Modifying the cell size should have little effect on the intrinsic energy resolution of the detector.
- Longitudinal sampling frequency: The longitudinal sampling frequency in the ECal was varied by changing the number of layers in the ECal while simultaneously changing the thicknesses of the layers such that the total depth, in radiation lengths, was held constant. Increasing the number of layers in a sampling calorimeter means any particles showering within it are sampled more, which leads to a reduction in the stochastic contribution to the energy resolution. Therefore, varying the number of layers is expected to change in intrinsic energy resolution of the calorimeter.
- Active material choice: The options under consideration for the active sensor material are silicon or plastic scintillator. As well as providing different intrinsic energy resolutions the readout mechanics of these two options are significantly different. There is no clear prior knowledge as to which should provide better performance.

2.2.1 ECal Cell Size

Different detector models were considered where the cell size in the ECal was varied about the nominal value of $5 \times 5 \text{ mm}^2$ square cells. The granularities considered were $3 \times 3 \text{ mm}^2$, $5 \times 5 \text{ mm}^2$, $7 \times 7 \text{ mm}^2$, $10 \times 10 \text{ mm}^2$, $15 \times 15 \text{ mm}^2$ and $20 \times 20 \text{ mm}^2$ square cells for both the silicon and scintillator active material options.

The energy resolution, using 100 GeV photons, as a function of the ECal cell size is shown in figure 2.2a for the silicon option and in figure 2.2b for the scintillator option. At this energy, the photons will be largely contained within the ECal and the reported energy resolution reflects solely the performance of the ECal. For both the silicon and scintillator ECal options the energy resolution does not depend strongly on the ECal cell size. This is to be expected as there is no change in the number of layers, which is the main factor in determining the energy resolution of a sampling calorimeter.

The only statistically significant variation observed occurs for the scintillator ECal option. A degradation in the energy resolution of $\sim 10\%$ is observed when reducing the ECal cell size from $5 \times 5 \text{ mm}^2$ to $3 \times 3 \text{ mm}^2$. The most likely cause is the "dead" region in the active material, which represents the readout multi pixel photon counter (MPPC) [13]. The MPPC occupies a fixed area of the cell, irrespective of cell size, and so the dead region of the cell fractionally increases as cell size is reduced. The larger this dead region, the worse the sampling of the electromagnetic showers in the ECal and the worse the resolution. While this effect will be present in all scintillator ECal options, it will only be significant for the small cell sizes when the dead region is fractionally the largest.

The ability to separate nearby electromagnetic particle showers within a calorimeter is limited by the Molière radius of the absorber material and the cell size. The Molière radius controls the width of the electromagnetic shower, while the cell size controls how the transverse shower profile is sampled. By reducing the cell size, it becomes easier to resolve nearby electromagnetic showers, which in turn reduces the effect of confusion. Therefore, it is expected that the jet energy resolution will be sensitive to the ECal cell size, even though the intrinsic energy resolution is not. The jet energy resolution as a function of ECal cell size is shown in figure 2.2a for the silicon option and figure 2.2b for the scintillator option. There is a strong dependance on the ECal cell size, with smaller cell sizes leading to lower values of the jet energy resolution; the jet energy resolution for 250 GeV jets for both ECal options goes from $\sim 3.0\%$ to $\sim 4.3\%$ when the ECal cell size goes from $3 \times 3 \text{ mm}^2$ to $20 \times 20 \text{ mm}^2$. The origin of this trend is best illustrated by

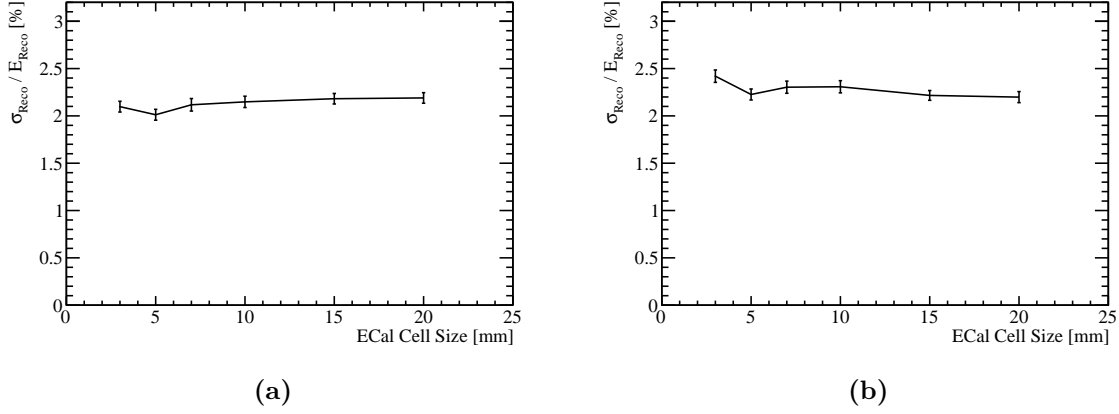


Figure 2.1: The energy resolution as a function of ECal cell size for 100 GeV photons using the nominal ILD detector model with (a) the silicon and (b) the scintillator ECal option.

considering the intrinsic energy resolution and confusion contributions to the jet energy resolution. These contributions are shown as a function of ECal cell size for 45 and 250 GeV jets in figure 2.3. It is clear from these contributions that the intrinsic energy resolution of the detector does not change when varying the cell size, which agrees with both prior expectations of calorimeter behaviour and the single particle energy resolution study. As expected, it can be seen that the trend in jet energy resolution as a function of the ECal cell size is being driven purely by changes to the confusion contribution and, in particular, the confusion caused by the reconstruction of photons.

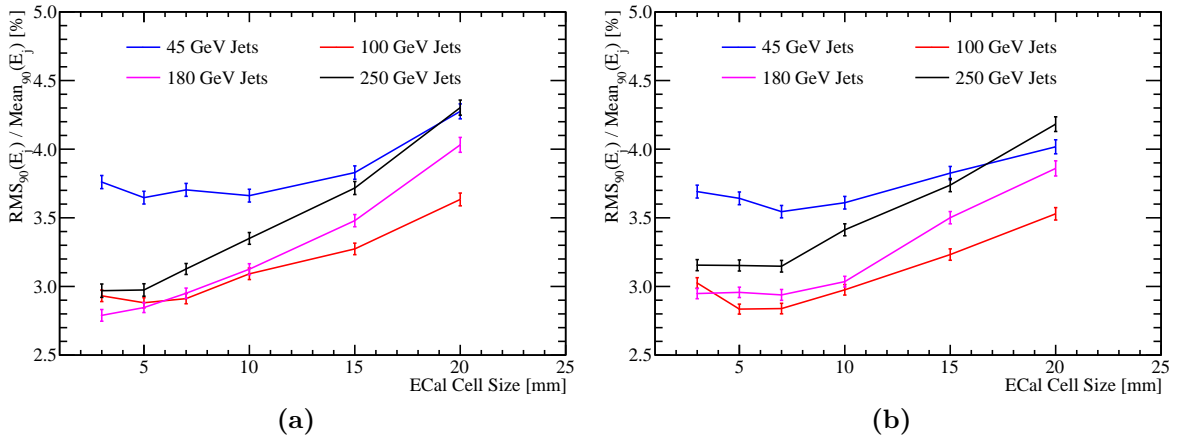


Figure 2.2: The fractional jet energy resolution as a function of ECal cell size for various jet energies using the nominal ILD detector model with (a) the silicon and (b) the scintillator ECal option.

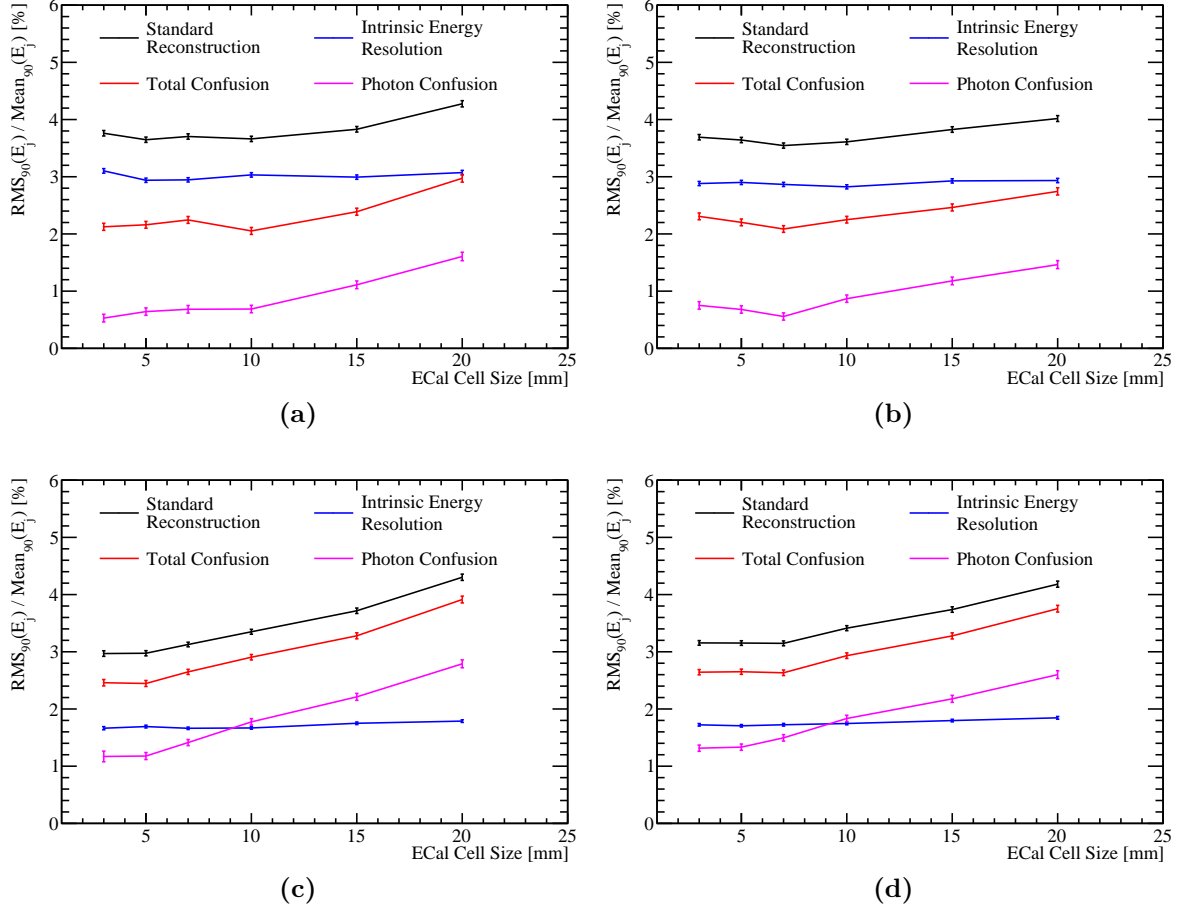


Figure 2.3: Contributions to the jet energy resolution shown as function of ECal cell size using the nominal ILD detector model for (a) the silicon ECal option and 45 GeV jets, (b) the scintillator ECal option and 45 GeV jets, (c) the silicon ECal option and 250 GeV jets and (d) the scintillator ECal option and 250 GeV jets. The black curves correspond to the standard reconstruction, the blue curves to the intrinsic energy resolution contribution to the jet energy resolution, the red curves to the confusion contribution to the jet energy resolution and the magenta curves to the confusion contribution to the jet energy resolution related solely to photon reconstruction

It is clear that the ECal cell size is extremely important for jet energy measurements, although it has little bearing on the intrinsic energy resolution of the ECal. Separation of the hadronic decays of the W and Z bosons, i.e. $\sigma_E/E \lesssim 3.8\%$ [4], can be achieved across the jet energy range considered here using a maximum ECal cell size of $15 \times 15 \text{ mm}^2$. However, as reducing the ECal cell size further continues to benefit the jet energy resolution, minimising the ECal cell size is desirable.

2.2.2 ECal Longitudinal Sampling Frequency

The detector performance was simulated where the number of layers in the ECal was varied, while keeping the total material budget (X_0) approximately constant. This study was performed for both the silicon and scintillator active material options. In all cases tungsten was used for the ECal absorber material and the active layer thicknesses were not changed from those used in the nominal ILD ECal summarised in table 2.1. The different ECal layouts considered are summarised in table 2.2.

Total Number of Layers $N_{\text{Layers ECal}}$	N_{Layers} Region 1	Absorber Thickness Region 1 [mm]	N_{Layers} Region 2	Absorber Thickness Region 2 [mm]	Total Thickness [X_0]
30	20	2.10	9	4.20	22.77
26	17	2.40	8	4.80	22.60
20	13	3.15	6	6.30	22.47
16	10	4.00	5	8.00	22.31

Table 2.2: The longitudinal structure of the ECal models considered in the optimisation study. The radiation length of tungsten absorber is 3.504 mm [14]. Note that a presampler layer contributes one extra layer to the cumulative number of layers.

The energy resolution, for 100 GeV photons, as a function of the number of layers in the ECal is shown in figure 2.4a for the silicon option and in figure 2.4b for the scintillator option. When the number of layers is increased σ_E/E decreases, which is expected because the energy resolution for a sampling calorimeter is $\propto 1/\sqrt{E \times N_{\text{Layers}}}$, where E is the reconstructed energy and N_{Layers} is the number of layers in the calorimeter.

When the number of layers in the ECal is increased, the intrinsic energy resolution benefits; the intrinsic energy resolution of the ECal improves by $\sim 25\%$ in both ECal options when increasing the number of layers from 16 to 30. This has the knock-on effect of reducing the confusion contribution to the jet energy resolution, which can be seen in figures 2.5a and 2.5b for the silicon and scintillator ECal options respectively. In both cases, the jet energy resolution was found to improve when the number of layers in the ECal was increased; the jet energy resolution goes from ~ 4.4 to $\sim 3.6\%$ for the silicon option and from ~ 4.1 to $\sim 3.6\%$ for the scintillator option when increasing the number of layers from 16 to 30. The magnitude of the change in jet energy resolution is dependent upon the jet energy, with a stronger dependency being observed for low

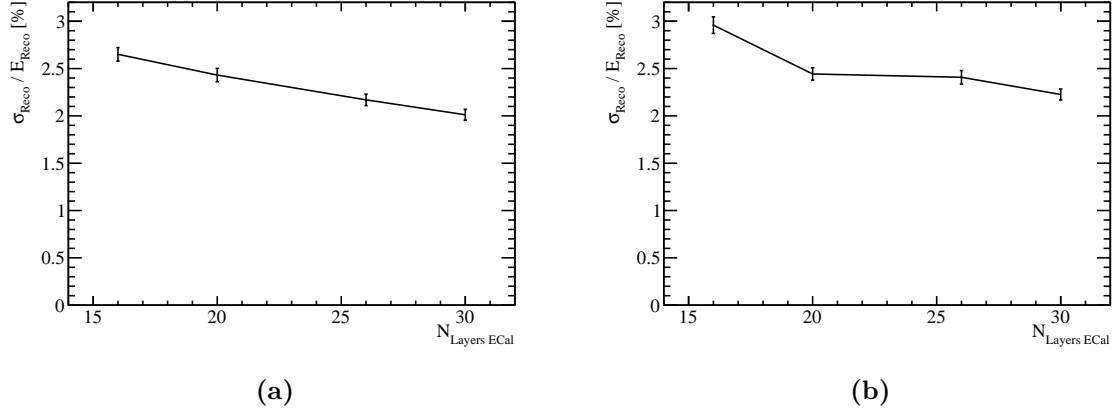


Figure 2.4: The energy resolution as a function of number of layers in the ECal for 100 GeV photons using the nominal ILD detector model with (a) the silicon and (b) the scintillator ECal option.

energy jets. This is expected from the stochastic contribution to the energy resolution for a sampling calorimeter. For high jet energies, changing the number of layers in the ECal does not significantly affect the jet energy resolution because the jet energy resolution is dominated by confusion. For low jet energies, the stochastic contribution to the energy resolution is bigger making it possible to resolve the changes to it when varying the number of layers in the ECal.

The decomposition of the jet energy resolution into the intrinsic energy resolution and confusion contributions for 45 and 250 GeV jets are shown, for both the silicon and scintillator ECal options, in figure 2.6. As expected, the improvement to the intrinsic energy resolution seen when increasing the number of layers in the ECal leads to the knock-on effect of lowering the confusion. However, significantly the magnitude of the change to the intrinsic energy resolution and confusion contributions to the jet energy resolution when varying the number of layers in the ECal are comparable in size. This shows that pattern recognition is as important for detector performance in the particle flow paradigm than intrinsic energy resolution.

2.2.3 ECal Active Material

In sections 2.2.1 and 2.2.2 the performance of the ECal was reported for both the silicon and scintillator options and to a large extent the performance of the two options was similar, but not identical:

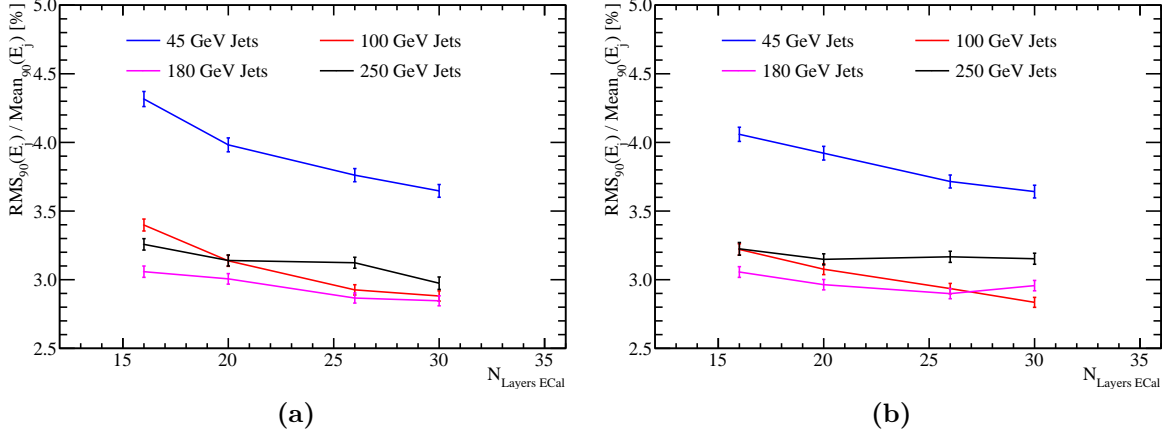


Figure 2.5: The jet energy resolution as a function of number of layers in the ECal for various jet energies using the nominal ILD detector model with (a) the silicon and (b) the scintillator ECal option.

- The intrinsic energy resolution of the silicon ECal option is better than that of the scintillator option at very high energies. For 500 GeV photons the intrinsic energy resolution is $\sim 25\%$ better for the silicon option. Section ?? contains a comparison between the photon energy resolution for the two ECal options, which clearly illustrates this. The most likely origin of the differing energy resolutions is the implementation of Birks' law [15] for scintillator active materials, which states

$$d\mathcal{L}/dx \propto \frac{dE/dx}{1 + k_B dE/dx} , \quad (2.1)$$

where $d\mathcal{L}/dx$ is the scintillation light yield per unit path length, dE/dx is the energy deposited per unit path length and k_B is a material property constant. For large energy deposits per unit length, such as those found in high energy photons, the light yield saturates causing a degradation in the energy resolution. When comparing the photon energy resolution for the silicon and scintillator ILD ECal options, which can be found in section ??, the saturation effect starts to degrade the energy resolution for the scintillator option around 50 GeV. However, the degradation in energy resolution is relatively small event up to 100 GeV.

- The "dead" region due to the presence of the MPPC in the simulation of the scintillator ECal option degrades performance of the detector for small transverse granularities, see figure 2.1.

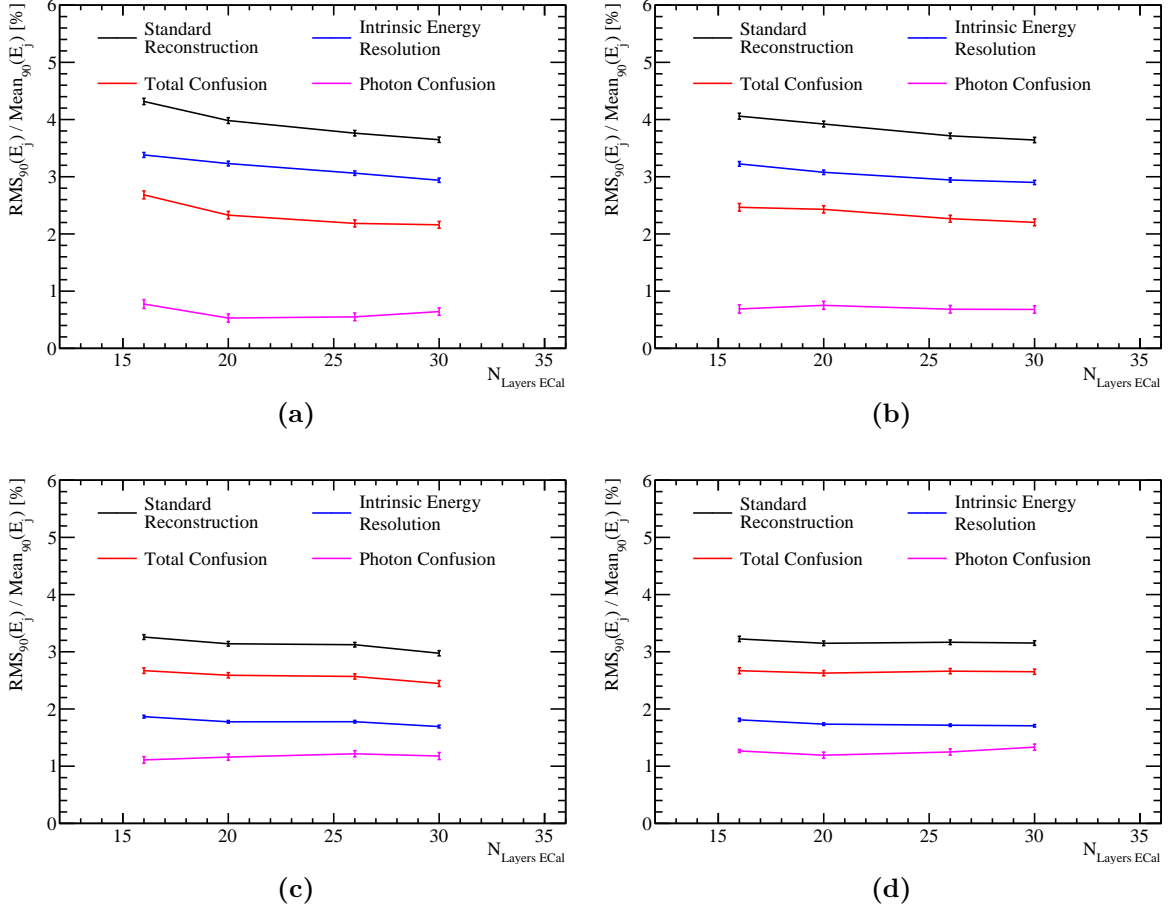


Figure 2.6: Contributions to the jet energy resolution shown as function of number of layers in the ECal using the nominal ILD detector model for (a) the silicon ECal option and 45 GeV jets, (b) the scintillator ECal option and 45 GeV jets, (c) the silicon ECal option and 250 GeV jets and (d) the scintillator ECal option and 250 GeV jets. The black curves correspond to the standard reconstruction, the blue curves to the intrinsic energy resolution contribution to the jet energy resolution, the red curves to the confusion contribution to the jet energy resolution and the magenta curves to the confusion contribution to the jet energy resolution related solely to photon reconstruction.

In summary, the performance of the two options, in terms of energy and jet energy resolution, at ILC-like energies is comparable. However, the silicon option is preferred when manufacture and implementation of the two models is compared. While constructing silicon wafers to fit a $5 \times 5 \text{ mm}^2$ square cell size is achievable, this would be extremely challenging for scintillator tiles. To resolve this in actuality, the scintillator ECal option would have to use $5 \times 45 \text{ mm}^2$ scintillator strips that are arranged in alternating directions in each ECal layer [1]. By combining information from neighbouring layers it becomes possible to approach an effective $5 \times 5 \text{ mm}^2$ square cell size.

2.3 Hadronic Calorimeter Optimisation

The purpose of an hadronic calorimeter (HCal) is to measure the energy deposits from hadronic showers. The HCal in the default ILD detector model, summarised in table 2.3, is approximately 6 nuclear interaction lengths (λ_I) deep. The ECal contributes approximately one λ_I giving a total of $\approx 7\lambda_I$, which is sufficient to contain jets at ILC like energies. The longitudinal structure of this model consists of 48 readout layers each containing a 3 mm active layer of scintillator and a 20 mm absorber layer of iron.

Parameter	Default Value
Cell Size	$30 \times 30 \text{ mm}^2$ square cells
Number of Layers	48 readout layers
Active Material Choice	Scintillator
Active Material Thickness	3 mm
Absorber Material Choice	Steel
Absorber Material Thickness	20 mm

Table 2.3: The configuration of the HCal in the nominal ILD detector model [1].

There are several readout approaches under consideration for the HCal including fully analogue, fully digital and semi-digital. Analogue readout reports the energy within each HCal cell using a continuous variable, while digital readout only produces a response if the energy deposited within a calorimeter cell is above a given threshold. The semi-digital approach mirrors that of the digital approach, but has three responses each with a different energy threshold. While the energy resolution for digital calorimeters is not as good as that of analogue calorimeters, it is possible to construct smaller cell sizes using a digital readout. In traditional calorimetry, a digital calorimeter would give a worse jet energy resolution than the analogue equivalent, however, that is not necessarily the case in particle flow calorimetry. If a digital calorimeter could be realised with a much smaller cell size than the analogue equivalent, then the effect of confusion in the digital calorimeter may be reduced such that it compensates for any loss to intrinsic energy resolution. In the following studies only the optimisation of the analogue HCal is presented as this is the readout approach used in the nominal ILD detector model.

A number of options were simulated where the following parameters in the HCal were varied:

- Cell size: This is crucial for successful application particle flow calorimetry for making associations between clusters of calorimeter hits and charged particle tracks. It is expected that the intrinsic energy resolution be invariant to changes in the HCal cell size.
- Number of readout layers: The number of layers in the HCal are varied, however, the thickness of those layers match those of the nominal ILD HCal design. This means the total depth of the HCal in λ_I is changing. It is expected that this study will determine the effect of leakage of energy out of the back of the HCal.
- Longitudinal sampling frequency: This involves changing the number of readout layers in the HCal while simultaneously changing the thicknesses of the active and absorber layers to keep the total number of λ_I in the HCal constant. As this modifies the sampling of particle showers in the HCal, it will affect the intrinsic energy resolution of the HCal.
- Sampling fraction: This is the ratio of the active medium thickness to the absorber medium thickness. This controls how particle showers within the calorimeter are sampled. In this study the total depth of the HCal in λ_I is held constant between detector models.
- Absorber material choice: Two options have been considered: steel and tungsten. This choice affects the growth and propagation of hadronic showers.

2.3.1 HCal Cell Size

The HCal cell size is an important detector parameter in the application of particle flow calorimetry. Smaller HCal cell sizes will lead to a finer spatial resolution that can be used to better separate charged and neutral particle calorimetric energy deposits. On the other hand, this will also lead to an increase in the number of readout channels that will raise the cost of the calorimeter. Therefore, it is highly desirable to achieve the optimal physics performance using the largest cell size possible. The nominal ILD HCal has a 30 mm square cell size and in this study the following cell sizes were considered; $10 \times 10 \text{ mm}^2$, $20 \times 20 \text{ mm}^2$, $30 \times 30 \text{ mm}^2$, $40 \times 40 \text{ mm}^2$, $50 \times 50 \text{ mm}^2$ and $100 \times 100 \text{ mm}^2$.

In the nominal ILD detector, 50 GeV long-lived neutral kaons (K_L^0 s) will deposit $\sim 65\%$ of their energy in the HCal and $\sim 35\%$ in the ECal. As 50 GeV K_L^0 s deposit the bulk of their energy in the HCal, they are appropriate to use when determining

the performance of the HCal. However, it should be emphasised that the K_L^0 energy resolutions represent the intrinsic energy resolution of the whole ILD detector and not purely that of the HCal.

Figure 2.7 shows the energy resolution for 50 GeV K_L^0 s as a function of cell size. As expected, the hadronic energy resolution does not strongly depend on the HCal cell size. The only statistically significant variation in energy resolution is observed for the $100 \times 100 \text{ mm}^2$ HCal cell size. For this model the energy resolution gets worse by $\sim 8\%$ in comparison to the other models considered. The most likely cause of this is a reduction in the effectiveness of the HCal hit energy truncation, which is described in section 1.3.1. The reduced effectiveness is expected because the precision used when obtaining the optimal energy truncation becomes worse as HCal cell size diverges from the nominal value.

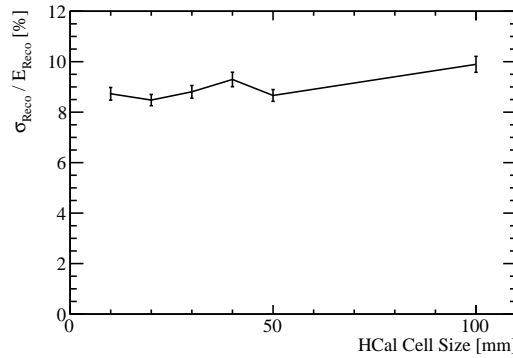


Figure 2.7: The energy resolution as a function of HCal cell size for 50 GeV K_L^0 events using the nominal ILD detector model.

A smaller HCal cell size will lead to better separation of charged and neutral hadron calorimetric energy deposits, therefore, it is expected that the confusion contribution to the jet energy resolution will be reduced by using smaller HCal cell sizes. Figure 2.8 shows the jet energy resolution as a function of cell size in the HCal. At low jet energies there is no strong dependency of the jet energy resolution on the HCal cell size, which is as expected from the K_L^0 energy resolution study. For high energy jets there is a clear dependence, with lower HCal cell sizes leading to better jet energy resolutions; the jet energy resolution for 250 GeV jets goes from $\sim 2.7\%$ to $\sim 3.5\%$ when the HCal cell size is increased from $10 \times 10 \text{ mm}^2$ to $100 \times 100 \text{ mm}^2$. Examining the different contributions to the jet energy resolution, shown in figure 2.9 it can be seen that the intrinsic energy resolution contribution does not depend on the HCal cell size; it is the confusion contribution that drives the overall trend in the jet energy resolution.

This is particularly clear at high jet energies where the confusion contribution to the jet energy resolution dominates that of the intrinsic energy resolution contribution. At high jet energies smaller HCal cell sizes leads to a reduction in the effect of confusion; the confusion contribution to the jet energy resolution is reduced by $\sim 25\%$ when reducing the HCal cell size from $100 \times 100 \text{ mm}^2$ to $10 \times 10 \text{ mm}^2$. At low jet energies the trend is less clear, as the confusion contribution is less dominant. Nevertheless, a reduction in the effect of confusion with decreasing cell size is still visible for all but the smallest HCal cell size. The most likely cause of the increase in confusion for the smallest HCal cell size at low energies is the tuning of the PandoraPFA algorithms to the nominal ILD HCal cell size. For both the 45 and 250 GeV jets, the photon confusion does not depend on the HCal cell size. This indicates that changes to the confusion term seen when varying the HCal cell size are related solely to the reconstruction of hadrons.

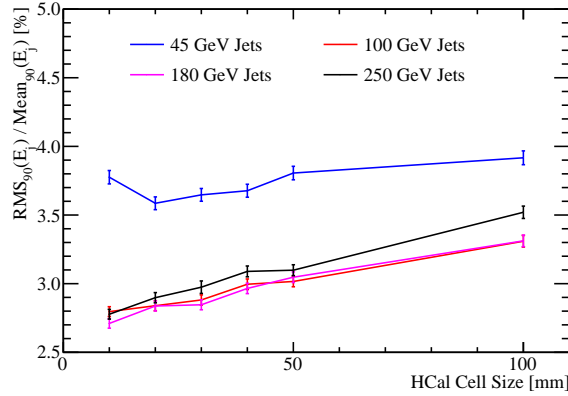


Figure 2.8: The jet energy resolution as a function of HCal cell size for various jet energies using the nominal ILD detector model.

A comparison of the results from the ECal and HCal cell size optimisation studies shows that the jet energy resolution has a stronger dependency on the ECal cell size than on the HCal cell size; increasing the nominal ECal cell size by a factor of three makes the jet energy resolution for 250 GeV jets worse by $\sim 20\%$, while increasing the nominal HCal cell size by the same factor makes the jet energy resolution worse by $\sim 12\%$. This is to be expected as in the particle flow paradigm $\approx 30\%$ of jet energy is recorded in the ECal, while only $\approx 10\%$ is recorded in the HCal. Consequently, the potential effect of double counting and omitting energy deposits, i.e. confusion, is greater in the ECal than the HCal. Therefore, minimising confusion in the ECal is expected to be more crucial for the overall jet energy resolution, which is what is observed. Furthermore, as PandoraPFA groups calorimeter hits together using a cone clustering approach, identifying the start of a particle shower is key for determining how calorimeter hits are grouped together deeper

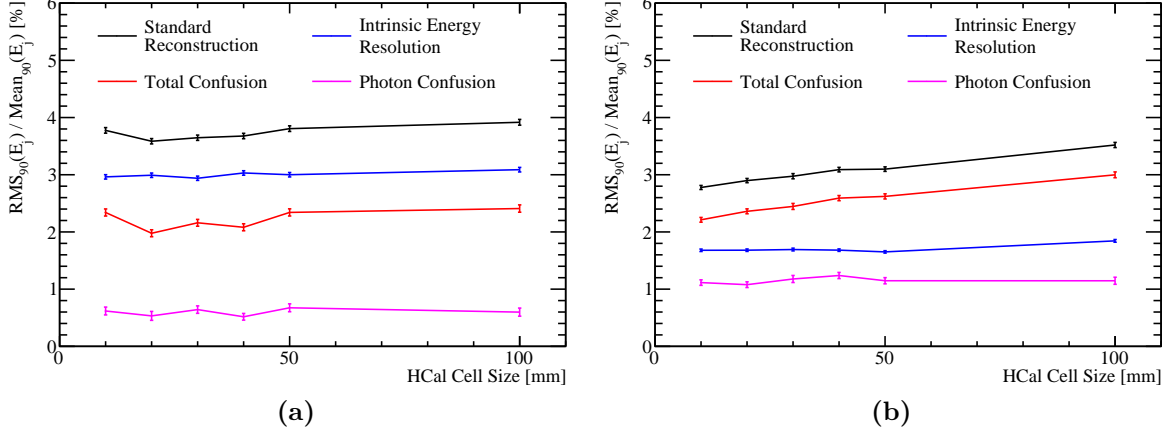


Figure 2.9: Contributions to the jet energy resolution shown as function of HCal cell size using the nominal ILD detector model for (a) 45 GeV jets and (b) 250 GeV jets. The black curves correspond to the standard reconstruction, the blue curves to the intrinsic energy resolution contribution to the jet energy resolution, the red curves to the confusion contribution to the jet energy resolution and the magenta curves to the confusion contribution to the jet energy resolution related solely to photon reconstruction.

into the calorimeters. In effect, this means the grouping of calorimeter hits in the HCal depends upon information gathered in the ECal. Therefore, if the ECal performance is sufficiently good, even with coarse HCal cell sizes, excellent performance can be achieved.

In summary, the confusion contribution to the jet energy resolution falls as the HCal cell size is reduced, while the intrinsic energy resolution of the detector is largely unaffected. As this dependancy is relatively weak, even the use of $100 \times 100 \text{ mm}^2$ HCal cell sizes would be enough to allow for separation of the hadronic decays of W and Z bosons, i.e. $\sigma_E/E \lesssim 3.8\%$ [4], at ILC like energies. However, there are benefits to having smaller HCal cell size; the jet energy resolution is reduced from $\sim 3.5\%$ to $\sim 2.8\%$ for 250 GeV jets when decreasing the HCal cell size from $100 \times 100 \text{ mm}^2$ to $10 \times 10 \text{ mm}^2$.

2.3.2 HCal Number of Layers

In this study, the total number of layers in the HCal was varied. In contrast to the longitudinal sampling frequency study, the active and absorber layer thicknesses in the HCal were not altered. Changing the number of layers in this way leads to a change in the total thickness of the calorimeter. This study is sensitive to the effects, if any, of leakage of energy out of the back of the calorimeters. The manufacturing cost of the HCal

is proportional to the number of readout channels and layers. Therefore, minimising the number of layers, while retaining excellent physics performance is important. Here detector models were simulated with a HCal containing 36, 42, 48 (nominal), 54 and 60 layers.

It is expected that the energy resolution of the detector will improve when the number of layers in the HCal is increased since fewer events should suffer from the effects of leakage. Any improvements seen by increasing the number of layers in the HCal is expected only up to the point where the majority of hadronic showers are fully contained by the calorimeters. The energy resolution as a function of number of layers in the HCal for 50 GeV K_L^0 is shown in figure 2.10. The energy resolution becomes worse as the number of layers in the HCal is reduced below 48 layers, while above this point additional layers do not change the energy resolution. This indicates that the majority of hadronic showers at this energy are fully contained by a 48 layer HCal. As reducing the number of HCal layers to 36 only causes a small degradation, $\sim 10\%$, in the neutral hadron energy resolution, it is feasible to consider reducing the number of layers in the ILD HCal.

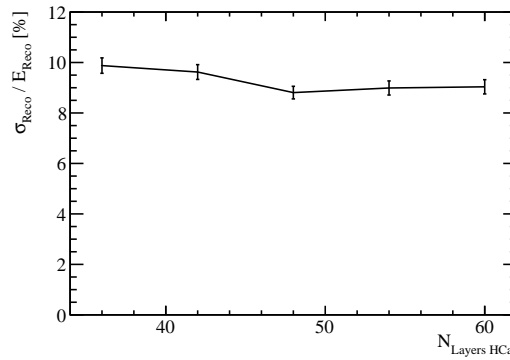


Figure 2.10: The energy resolution as a function of number of layers in the HCal for 50 GeV K_L^0 events using the nominal ILD detector model.

Figure 2.11 shows the jet energy resolution as a function of the number of layers in the HCal. For low energy jets, where intrinsic energy resolution dominates, the jet energy resolution does not depend on the number of layers in the HCal. At high jet energies, where confusion dominates, increasing the number of layers in the HCal improves the jet energy resolution; the jet energy resolution goes from $\sim 3.4\%$ to $\sim 3.0\%$ for 250 GeV jets when increasing the number of HCal layers from 36 to 48. The origin of these trends is leakage of energy out of the back of the calorimeters, which becomes more problematic as the number of layers in the HCal is reduced and the jet energy increases.

Figure 2.12 shows the jet energy resolution contributions as a function of the number of layers in the HCal. These results appear somewhat counterintuitive in that the intrinsic energy resolution of the detector does not seem to depend on the number of layers in the HCal even for high energy jets. However, this is expected given only 10% of jet energy is carried in the form of neutral hadrons and the neutral hadron energy resolution, for 50 GeV hadrons, is only weakly dependent on the number of HCal layers. Leakage does have an effect on the intrinsic energy resolution, however, the use of RMS_{90} obscures part of this by excluding events where leakage is significant. The fractional decrease in RMS_{90} for the intrinsic energy distribution when increasing the number of HCal layers from 36 to 60 is $\sim 4\%$, however, the change in the full RMS is $\sim 23\%$. Figure 2.12 also shows that the confusion contribution is far more sensitive to the number of layers in the HCal than the intrinsic energy resolution. This sensitivity originates from the reclustering stage of the reconstruction in events where leakage has occurred. In these events, when PandoraPFA compares the momentum of a charged particle track to the cluster of calorimeter hits that it produces, there will be a disparity. To resolve the disparity, PandoraPFA will associate other calorimeter energy deposits that were not produced by the charged particle to the track to compensate for the leaked energy, which produces confusion. As photons are largely contained within the ECal at these energies, the photon confusion contribution to the jet energy resolution has no dependence on the number of layers in the HCal.

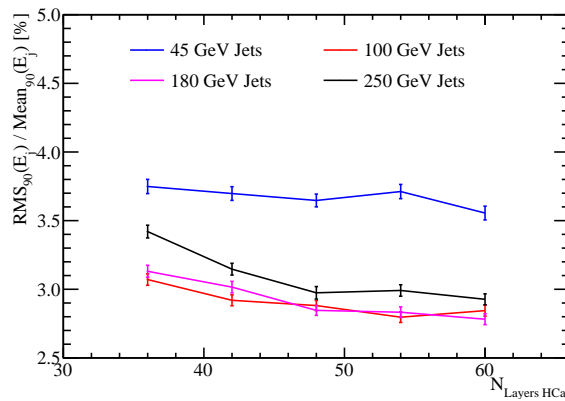


Figure 2.11: The jet energy resolution as a function of number of layers in the HCal for various jet energies using the nominal ILD detector model.

In summary, even if the number of layers in the HCal were reduced by 25%, the jet energy resolution would be sufficient for separating the hadronic decays of the W and Z bosons at ILC energies, i.e. $\sigma_E/E \lesssim 3.8\%$ [4]. Although, the effects of leakage do make the jet energy resolution worse for ILC like energies, once the number of layers in the

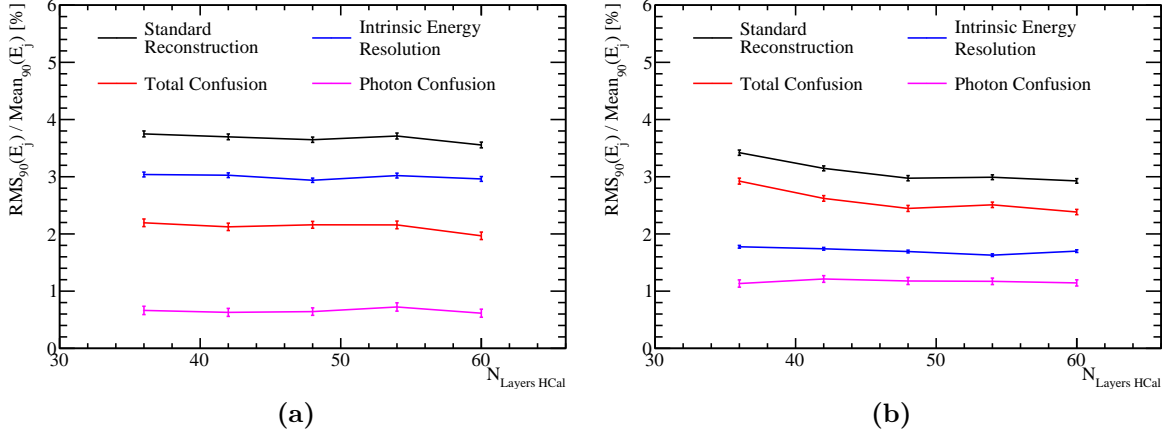


Figure 2.12: Contributions to the jet energy resolution shown as function of number of layers in the HCal using the nominal ILD detector model for (a) 45 GeV jets and (b) 250 GeV jets. The black curves correspond to the standard reconstruction, the blue curves to the intrinsic energy resolution contribution to the jet energy resolution, the red curves to the confusion contribution to the jet energy resolution and the magenta curves to the confusion contribution to the jet energy resolution related solely to photon reconstruction.

HCal is reduced from 48 layers, therefore, it is desirable to have a minimum of 48 layers in the ILD HCal.

2.3.3 HCal Longitudinal Sampling Frequency

Several detector models were simulated where the longitudinal sampling frequency in the HCal was modified. The longitudinal sampling frequency was altered by changing the number of layers in the HCal, while simultaneously changing the active and absorber layer thicknesses, to maintain the total number of nuclear interaction lengths. For each model considered, the absorber material was steel, containing a total of $5.72 \lambda_I$, and the active material was scintillator, containing a total of $0.19 \lambda_I$. The ratio of the active to absorber layers thicknesses (the sampling fraction) in these models is the same as in the nominal ILD HCal. A summary of the detector models considered is given in table 2.4.

Figure 2.13 shows the energy resolution for 50 GeV K_L^0 as a function of number of layers in the HCal. As the number of layers in the HCal is increased, the energy resolution improves. This is because increasing the number of layers in a sampling calorimeter, while leaving the total material budget unchanged, will lead to greater sampling of particles

Number $N_{\text{Layers HCal}}$	Absorber Thickness [mm]	Active Thickness [mm]
60	16.00	2.40
54	17.78	2.67
48	20.00	3.00
42	22.86	3.43
36	26.67	4.00
30	32.00	4.80
24	40.00	6.00
18	53.33	8.00

Table 2.4: Longitudinal configuration of the HCal in the detector models considered.

showering within it and a reduction the stochastic contribution to the energy resolution. The energy resolution is less pronounced than the naive expectation of $1/N_{\text{HCal}}$, where N_{HCal} is the number of layers in the HCal, because this relationship only holds for the energy resolution of a single sampling calorimeter and these results are for the full ILD detector, including the $\approx 1\lambda_I$ in the ECal. Furthermore, the $1/N_{\text{HCal}}$ functional form neglects a number of effects, such as instrumentation defects and electrical noise, that should be included when parameterising the energy resolution [3].

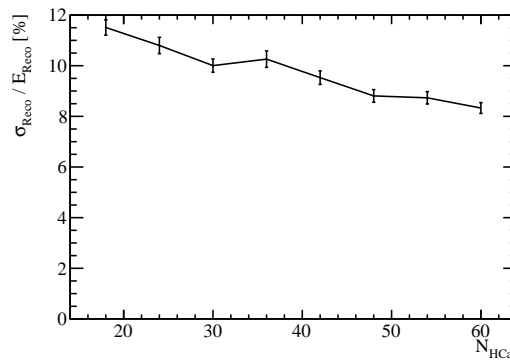


Figure 2.13: The energy resolution as a function of the longitudinal sampling frequency in the HCal for 50 GeV K_L^0 events using the nominal ILD detector model.

Figure 2.14 shows the jet energy resolution as a function of the longitudinal sampling frequency in the HCal. Increasing the number of layers in the HCal leads to an improvement in the HCal; when the number of layers in the HCal is increased from 18 to 60 the jet energy resolution for 250 GeV jets improves by $\sim 17\%$.

Figure 2.15 shows that both the intrinsic energy resolution and confusion improve with increasing longitudinal sampling frequency. For 250 GeV jets, when increasing the number of HCal layers from 18 to 60 the intrinsic energy resolution contribution goes from $\sim 1.9\%$ to $\sim 1.6\%$ and the confusion contribution goes from $\sim 3.0\%$ to $\sim 2.4\%$. The twofold improvement is expected because increasing the longitudinal sampling frequency improves the intrinsic energy resolution of a sampling calorimeter, which has the knock-on effect of lowering the confusion. The resulting reduction in confusion is due to the improved precision obtained when comparing the momenta of charged particle tracks and the energy of clusters of calorimeter hits. These comparisons are used to guide event reconstruction in PandoraPFA, therefore, if the precision of these comparisons is improved, the confusion is reduced as described in section ??.

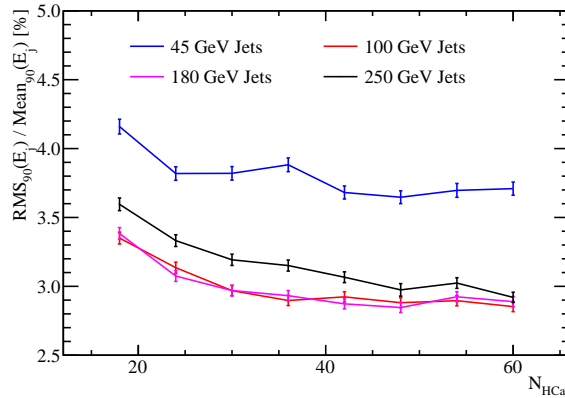


Figure 2.14: The jet energy resolution as a function of longitudinal sampling frequency in the HCal for various jet energies using the nominal ILD detector model.

It is clear that a larger number of layers in the HCal benefits both the intrinsic energy resolution of the ILD detector as well as reducing the confusion contribution to the jet energy resolution. As there are few physics analyses that rely on the identification and categorisation of individual neutral hadrons, but there are many that rely on identification and categorisation of photons, the intrinsic energy resolution of the HCal is less crucial from a physics perspective than that of the ECal. However, these studies show the HCal has a crucial role to play in jet reconstruction in the particle flow paradigm. To achieve a jet energy resolution of $\sigma_E/E \lesssim 3.8\%$ [4], which is required to separate the W and Z hadronic decays, the ILD detector will require a minimum of 42 layers in the HCal. This longitudinal sampling frequency is required particularly for low energy jets where the energy resolution is dominated by the intrinsic energy resolution of the detector.

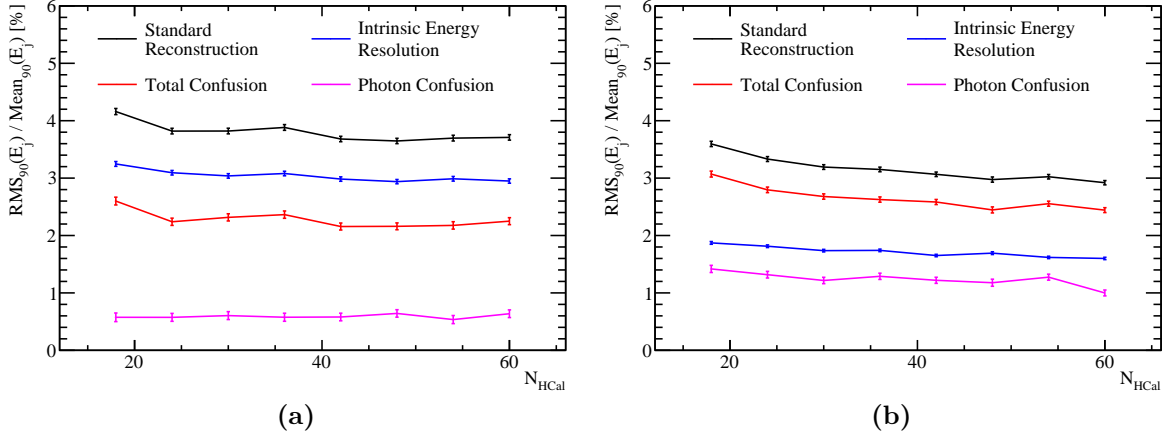


Figure 2.15: Contributions to the jet energy resolution shown as function of the longitudinal sampling frequency in the HCal using the nominal ILD detector model for (a) 45 GeV jets and (b) 250 GeV jets. The black curves correspond to the standard reconstruction, the blue curves to the intrinsic energy resolution contribution to the jet energy resolution, the red curves to the confusion contribution to the jet energy resolution and the magenta curves to the confusion contribution to the jet energy resolution related solely to photon reconstruction.

2.3.4 HCal Sampling Fraction

The performance of the ILD detector was studied for different ratios of active to absorber later thicknesses in the HCal. In the nominal detector model, the active scintillator layer thickness is 3 mm, while the absorber layer thickness is 20 mm giving a sampling fraction of 0.15. HCal models were simulated where this ratio was changed from 0.05 to 0.25 in steps of 0.05, while retaining the same number of interaction lengths.

No performance changes in the energy resolution for 50 GeV K_L^0 s or the jet energy resolution for 91, 200, 360 and 500 GeV $Z \rightarrow uds$ di-jet events were observed when varying the ratio of active to absorber later thicknesses. Based on these simulations, there is no suggestion that varying this ratio has any statistically significant effect on the physics performance. Although this study indicates that thinning the active layer thickness would not change performance, hardware effects must also be considered to determine whether these conclusions hold true in a real detector. A study into the effects of the readout electronics is required before changing the active layer thicknesses to determine whether a MIP signal can be clearly distinguished when changing the sampling fraction.

2.3.5 HCal Absorber Material

The nominal choice of HCal absorber material is steel with tungsten providing a feasible alternative [16]. Although tungsten is more expensive than steel, it contains a larger number of nuclear interaction lengths per unit length. Therefore, using tungsten as the absorber material would allow for a reduction in the size of the HCal, while retaining the same number of nuclear interaction lengths. Reducing the depth of the calorimeter would decrease the size of the solenoid required, which would offset some of the additional cost of tungsten.

Table 2.5 shows the configuration for the steel and tungsten HCal options that were used in the full ILD simulation. To isolate the effects of changing the absorber material, the total depth, in nuclear interaction lengths, was kept constant when comparing the two options. Furthermore, the sampling fraction was also held constant. A number of different physics lists exist within GEANT4 for the modelling of hadronic showers. The default model for high energy physics calorimetry is the QGSP_BERT physics list. This uses the quark-gluon string model [17] with the precompound model of nuclear evaporation [18] (QGSP) for high energy interactions and the Bertini (BERT) cascade model [19] for intermediate energy interactions. For the study of absorber materials both the QGSP_BERT and the QGSP_BERT_HP physics lists were used. The QGSP_BERT_HP list uses the high precision neutron package (NeutronHP) to deal with the transportation of neutrons from below 20 MeV to thermal energies. This added detail is necessary for accurate modelling of hadronic showers in tungsten [12].

Parameter	Steel HCal Option	Tungsten HCal Option
Cell Size	$30 \times 30 \text{ mm}^2$ square cells	$30 \times 30 \text{ mm}^2$ square cells
Number of Layers	48 readout layers	48 readout layers
Absorber Material Thickness [mm]	20.0	12.0
Active Material Choice	Scintillator	Scintillator
Active Material Thickness [mm]	3.0	1.8

Table 2.5: The configuration of the steel and tungsten HCal options [1].

One of the dominant processes governing the energy deposition of hadronic showers in calorimeters is spallation [7]. Spallation begins with the collision of a high energy incident particle with nucleons in the calorimeter absorber material. This collision creates a cascade of high energy hadronic particles, e.g. protons, neutrons and pions, are

produced within the nucleus. If these energies are large enough, some of these particles may escape the nucleus and form secondary particles in the hadronic shower. After this initial collision, the nuclei of the absorbing material are left in an excited state. Assuming the excited nuclei are sufficiently stable that they will not undergo fission, they will return to a stable state by ejecting energy in the form of particles in a process called evaporation. Evaporation of neutrons, which is the dominant form of evaporation, significantly delays the growth of hadronic showers as after the evaporation process some of these neutrons participate in neutron capture [12]. Neutron capture involves an absorber nuclei capturing a neutron and then emitting a photon as it returns to a stable state. The time taken for the neutron capture mechanism to proceed is limited by the lifetime of the unstable nuclei [20], which typically makes neutron capture one of the slowest mechanisms by which hadronic showers can propagate. The number of evaporation neutrons released in a hadronic shower increases with the atomic number, Z , of the absorber material of a calorimeter increases. This is because of the increase in neutron content of the absorber material nuclei [12]. As the number of evaporation neutrons increases, more neutron capture processes are initiated, which results in a longer hadronic shower development time. Figure 2.16 shows the shower development times for hadronic showers in the tungsten ($Z=74$) and steel (iron, $Z=26$) HCal options and, as expected, the shower development time is greater for tungsten.

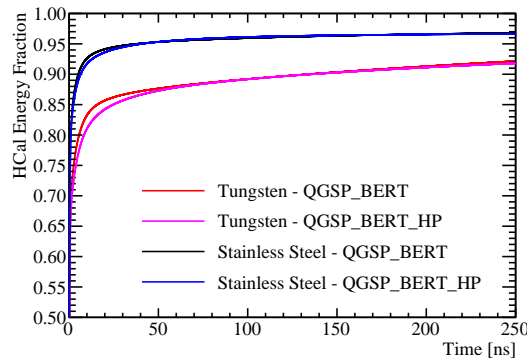


Figure 2.16: The fraction of the total calorimetric energy deposited in the HCal as a function of time for 25 GeV K_L^0 events using the steel and tungsten HCal options. Results are shown for both the QGSP_BERT and QGSP_BERT_HP physics lists. The calorimeter hit times have been corrected for straight line time of flight to the impact point.

Table 2.6 shows the energy resolution for 50 GeV K_L^0 s obtained using the nominal ILD detector model with various HCal absorber materials and GEANT4 physics lists. In comparison to steel, tungsten option offers a $\sim 8\%$ improvement in the energy resolution

for 50 GeV neutral hadrons (using the QGSP_BERT_HP physics list). This can be attributed to differences in the nuclear structure of the two materials, which will lead to different developments of the hadronic showers within them. For example, the energy losses to nuclear binding energies are smaller in tungsten than steel, as the target nucleons are less stable than in iron, therefore, less energy is needed to liberate them. This will lead to a larger signal for tungsten and a reduction in the energy resolution in comparison to steel. The results of table 2.6 also indicate that the addition of the high precision neutron package was not important for this study.

HCal Option	Energy Resolution [%]
Steel, QGSP_BERT	8.8 ± 0.2
Steel, QGSP_BERT_HP	9.0 ± 0.3
Tungsten, QGSP_BERT	8.3 ± 0.2
Tungsten, QGSP_BERT_HP	8.3 ± 0.2

Table 2.6: The energy resolution for 50 GeV K_L^0 s obtained using the nominal ILD detector with various HCal absorber materials and GEANT4 physics lists. A 100 ns timing cut was applied to the steel and tungsten HCal options in these simulations.

It should be emphasised that the HCal hit energy truncation, as described in chapter 1, used for the tungsten and steel HCal options differs because tungsten contains a larger number of radiation lengths per nuclear interaction length than steel does. As the HCal primarily measures hadronic showers, one may naively expect the number of radiation lengths in the HCal to be irrelevant, given both options have the same number of nuclear interaction lengths. However, this is not the case because all hadronic showers have an electromagnetic component generated by the decays of hadrons to photons, e.g. $\pi^0 \rightarrow \gamma\gamma$ and $\eta \rightarrow \gamma\gamma$. This leads to hadronic showers depositing more energy per calorimeter hit in tungsten than in steel and makes retuning the HCal hit energy truncation a necessity. As expected, the truncation used for tungsten, 5 GeV, is larger than for steel, 1 GeV, because of the increased average hit energy.

Table 2.7 shows the jet energy resolutions for selected jet energies obtained using the nominal ILD detector with various HCal absorber materials and GEANT4 physics lists. These results indicate that steel outperforms tungsten as the HCal absorber material. The magnitude of the improvement offered using steel grows as the jet energy increases; the jet energy resolution is $\sim 3\%$ better for the steel option for 45 GeV jets, while for 250 GeV jets the improvement is $\sim 11\%$. The intrinsic energy resolution and confusion

contributions to the jet energy resolution for 45 and 250 GeV jets are shown in table 2.8. The intrinsic energy resolution contribution to the jet energy resolution is almost identical for the two HCal options, which is expected because the K_L^0 energy resolution was only slightly better for the tungsten option. The tungsten option is unlikely to give a significantly better intrinsic energy resolution because only the small fraction of jet energy associated with neutral hadrons is measured in the HCal. The confusion contribution to the jet energy resolution is larger for tungsten than for steel; for 250 GeV jets the confusion contribution is $\sim 3.4\%$ in tungsten and only $\sim 3.0\%$ in steel. The larger confusion contribution is expected for the tungsten option because hadronic showers are generally wider in tungsten. The transverse profile of hadronic showers in the two HCal options is illustrated in figure 2.17, which shows the normalised distribution of the energy weighted transverse distance from the shower axis to the calorimeter hits for 50 GeV hadronic showers for both the steel and tungsten HCal options. Increasing the average hadronic shower width makes resolving individual particle showers in a dense jet environment more challenging, which means more calorimetric energy deposits will be incorrectly clustered together. This in turn results in incorrect associations being made between calorimetric energy deposits and charged particle tracks i.e. an increased confusion contribution. Again, the use of the QGSP_BERT_HP physics list, as opposed to QGSP_BERT, made a minimal impact on these results.

HCal Option	Jet Energy Resolution [%]			
	45 GeV	100 GeV	180 GeV	250 GeV
Steel, QGSP_BERT	3.65 ± 0.05	2.88 ± 0.04	2.85 ± 0.04	2.97 ± 0.05
Steel, QGSP_BERT_HP	3.67 ± 0.05	2.92 ± 0.04	2.86 ± 0.04	3.03 ± 0.04
Tungsten, QGSP_BERT	3.78 ± 0.05	3.12 ± 0.04	3.15 ± 0.04	3.43 ± 0.04
Tungsten, QGSP_BERT_HP	3.80 ± 0.05	3.08 ± 0.04	3.24 ± 0.04	3.41 ± 0.04

Table 2.7: The jet energy resolution for selected jet energies obtained using the nominal ILD detector with various HCal absorber materials and GEANT4 physics lists. A 100 ns timing cut was applied to the steel and tungsten HCal options in these simulations.

The impact of the choice of HCal absorber material is small on both the neutral hadron energy resolution and intrinsic energy resolution, however, the steel HCal option outperforms the tungsten option in terms of pattern recognition confusion. When examining the mechanical properties of steel and tungsten, it is clear that steel has a significant advantage over tungsten in terms of rigidity [2]. This means that fewer

HCal Option	Jet Energy Resolution [%]			
	45 GeV		250 GeV	
	Intrinsic	Confusion	Intrinsic	Confusion
Steel, QGSP_BERT	2.93 ± 0.04	2.16 ± 0.06	1.69 ± 0.02	2.45 ± 0.05
Steel, QGSP_BERT_HP	2.98 ± 0.04	2.15 ± 0.06	1.65 ± 0.02	2.53 ± 0.04
Tungsten, QGSP_BERT	2.97 ± 0.04	2.34 ± 0.06	1.65 ± 0.02	3.01 ± 0.05
Tungsten, QGSP_BERT_HP	2.92 ± 0.04	2.42 ± 0.06	1.65 ± 0.02	2.99 ± 0.05

Table 2.8: The contributions to the jet energy resolution obtained using the nominal ILD detector with various HCal absorber materials and GEANT4 physics lists. A 100 ns timing cut was applied to the steel and tungsten HCal options in these simulations.

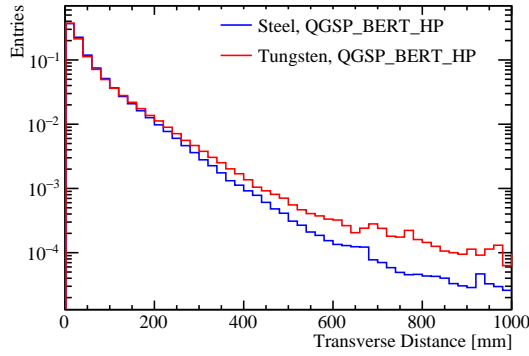


Figure 2.17: The normalised distribution of the energy weighted transverse distance of the calorimeter hits from a 50 GeV hadronic shower to the shower axis. The blue and red lines show the energy weighted transverse distance obtained using a steel and tungsten HCal absorber material in the ILD detector respectively. The simulations used the QGSP_BERT_HP physics list.

support structures would be required for the calorimeter leading to less dead material and better performance, which makes steel the preferred option.

2.4 Global Detector Parameters

The overall detector size and the magnetic field strength are major cost drivers for the ILD detector. Both will affect the jet energy resolution and studies showing their impact on detector performance are presented here.

2.4.1 The Magnetic Field Strength

In the particle flow paradigm the momentum of charged particles is obtained through the curvature of their trajectory as they bend in the magnetic field. Therefore, the magnetic field is an integral element for the successful application of particle flow calorimetry. Furthermore, the magnetic field deflects charged particles away from neutral particles in jets. The stronger the magnetic field, the larger the average separation between the calorimetric energy deposits made by charged and neutral particles in jets, which reduces the effect of confusion. Therefore, it is expected that a stronger magnetic field will lead to better jet energy resolutions through a reduction of the confusion contribution to the jet energy resolution.

Detector models were simulated where the magnetic field was varied from 1.0 to 5.0 T in steps of 0.5 T and the resulting jet energy resolutions are shown in figure 2.18. The larger the magnetic field strength, the better the jet energy resolution. Increasing the magnetic field strength from 1.0 to 5.0 T improves the jet energy resolution for 250 GeV jets by $\sim 25\%$. The higher the jet energy, the stronger the dependence of the jet energy resolution on the magnetic field strength.

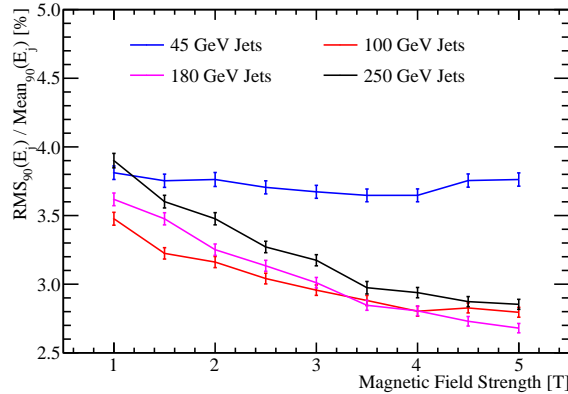


Figure 2.18: The jet energy resolution using the nominal ILD detector as a function of the magnetic field strength for various jet energies.

Figure 2.19 shows the breakdown of the jet energy resolution into the various contributions. As expected, there is a reduction in the confusion contribution with increasing magnetic field strength. Furthermore, there is a reduction in intrinsic energy resolution with increasing magnetic field strength for low energy jets. This is most likely due to particles being directed into the forward region of the detector. When a charged particle passes through a magnetic field it will, assuming no energy losses, traverse a helix. The

radius of curvature, R , of that helix is given by

$$R = \frac{p_T}{qB}, \quad (2.2)$$

where p_T is the transverse momentum of the charged particle with respect to the magnetic field, q is the electric charge of the particle and B is the magnetic field strength. When the magnetic field strength increases, the radius of curvature for charged particles will decrease and more low charged particles will be directed toward the forward regions of the detector. As the tracking coverage in the forward region of the detector is worse in the central region [1], increasing the magnetic field strength leads to fewer charged particles being reconstructed, which is illustrated in figure 2.20, and a degradation in the energy resolution. For high jet energies, low transverse momentum charged particles will still get directed to the forward regions of the detector, however, these contribute fractionally less energy to the total reconstructed energy. Therefore, the trend of worsening intrinsic energy resolution with increasing magnetic field strength is less pronounced as the jet energy grows.

At high jet energies, reducing the magnetic field strength appears to degrade the intrinsic energy resolution; the intrinsic energy resolution for 250 GeV jets goes from $\sim 1.8\%$ to $\sim 2.1\%$ when reducing the magnetic field strength from 5.0 T to 1.0 T. This trend is due to an artefact in the definition of the intrinsic energy resolution for jets meaning it is not a genuine effect. The intrinsic energy resolution is highly non-trivial to determine; Monte-Carlo (MC) information is used to make all associations between charged particle tracks and clusters of calorimeter hits as follows:

1. Each calorimeter hit is associated to the MC particle that deposits the largest amount of energy in that hit;
2. Clusters of calorimeter hits formed by the same MC particle are clustered together;
3. Each charged particle track is associated to the MC particle that produced it;
4. Clusters of calorimeter hits are associated to charged particle tracks if they are made by the same MC particle.

This procedure assumes that only one MC particle deposits significant energy per calorimeter hit. If multiple MC particles deposit significant energy in the same calorimeter hit, this assumption breaks down and errors are made when associating charged particle tracks to calorimetric energy deposits. These errors cause the same double counting and

omission of energy deposits as confusion does, however, they have a smaller effect because multiple MC particles deposit significant energy in the same calorimeter hit is rare in finely segmented calorimeters. As the overlap of particle showers within the calorimeter grows, as it does for high energy jets when reducing the magnetic field, the intrinsic energy resolution appears to get worse because of this confusion-like effect. Because this effect is small in comparison to changes in the confusion contribution, the overall dependence of the detector performance on the magnetic field strength can be confidently quantified.

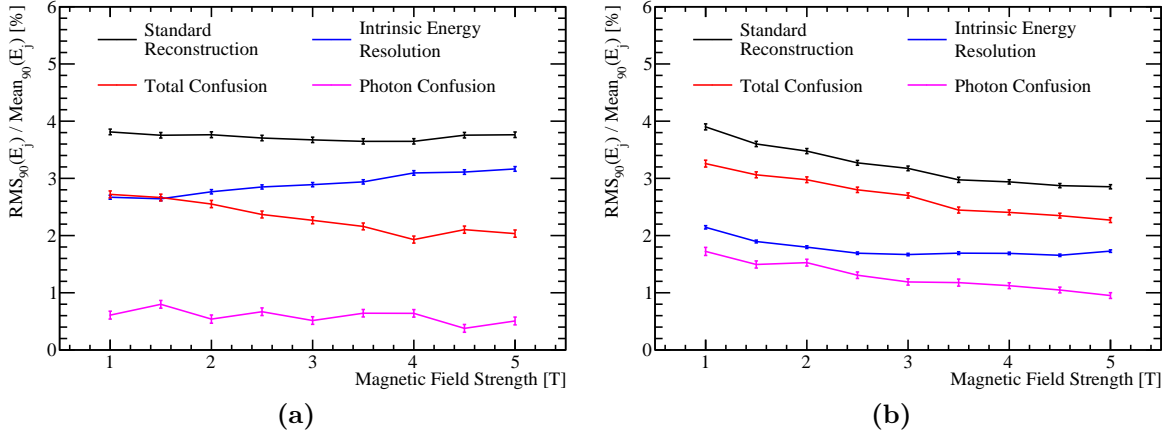


Figure 2.19: Contributions to the jet energy resolution shown as function of the magnetic field strength using the nominal ILD detector model for (a) 45 GeV jets and (b) 250 GeV jets. The black curves correspond to the standard reconstruction, the blue curves to the intrinsic energy resolution contribution to the jet energy resolution, the red curves to the confusion contribution to the jet energy resolution and the magenta curves to the confusion contribution to the jet energy resolution related solely to photon reconstruction.

In summary, increasing the magnetic field strength is beneficial to the jet energy resolution because it reduces confusion from associating tracks to calorimetric energy deposits from charged particles. The intrinsic energy resolution is also dependent upon the magnetic field strength, however, the effect is small in comparison to the confusion. Although a magnetic field of 1.5 T would give good enough performance to be able to separate the hadronic decays of W and Z bosons, i.e. $\sigma_E/E \lesssim 3.8\%$ [4], at the energies considered, increasing the field strength further significantly improves the detector performance.

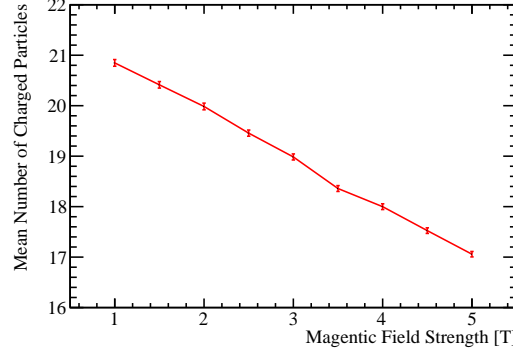


Figure 2.20: The mean number of reconstructed charged particles as a function of the magnetic field strength for 91 GeV $Z \rightarrow uds$ di-jet events. The nominal ILD detector model was used and the pattern recognition has been fully cheated using the MC information.

2.4.2 Inner ECal Radius

The impact on the jet energy resolution of the overall size of the detector was studied by simulating detector models where the ECal inner radius was altered. The ECal inner radii considered were 1208, 1408, 1608, 1808 (nominal) and 2008 mm.

Figure 2.21 shows the dependence of the jet energy resolution on the ECal inner radius. Increasing the ECal inner radius increases the separation between particles as they enter the calorimeters, which reduced the effect of confusion and improves the jet energy resolution. As confusion is more dominant at higher energies, the benefits to using a larger ECal radius grow with increasing jet energy; increasing the ECal inner radius from 1208 mm to 2008 mm improves the jet energy resolution by $\sim 9\%$ for 45 GeV jets, but by $\sim 25\%$ for 250 GeV jets. Figure 2.22 shows the decomposition of the jet energy resolution into its different component. These results explicitly show a reduction in confusion with increasing ECal inner radius; the confusion contribution goes from $\sim 3.4\%$ to $\sim 2.4\%$ when increasing the ECal inner radius from 1208 mm to 2008 mm. The intrinsic energy resolution of the detectors shows no strong dependence on the inner ECal radius. The apparent degradation in intrinsic energy resolution at low ECal inner radii is an artefact of the association of a single MC particle per calorimeter cell when running the cheated pattern recognition as explained in section 2.4.1. The dominant effect driving the jet energy resolution is, as expected, the confusion.

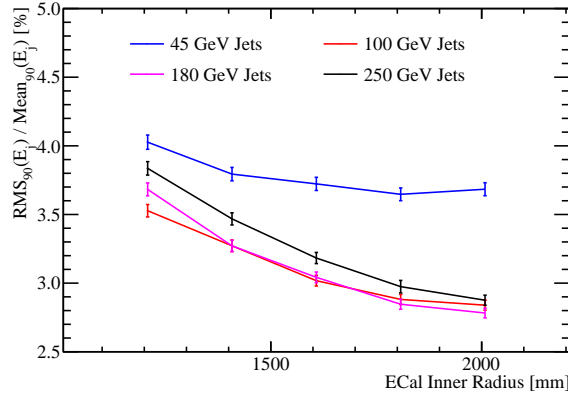


Figure 2.21: The jet energy resolution using the nominal ILD detector as a function of the ECal inner radius for various jet energies.

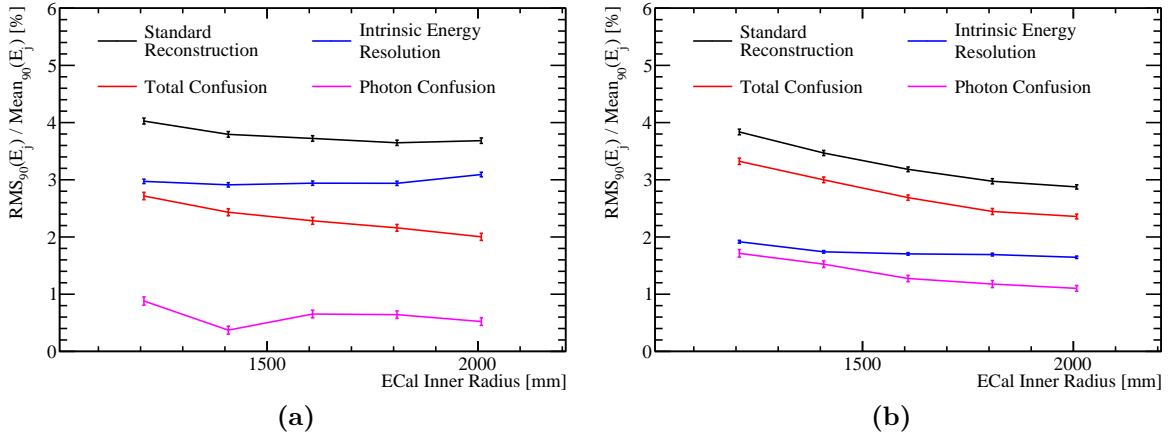


Figure 2.22: Contributions to the jet energy resolution shown as function of the ECal inner radius using the nominal ILD detector model for (a) 45 GeV jets and (b) 250 GeV jets. The black curves correspond to the standard reconstruction, the blue curves to the intrinsic energy resolution contribution to the jet energy resolution, the red curves to the confusion contribution to the jet energy resolution and the magenta curves to the confusion contribution to the jet energy resolution related solely to photon reconstruction.

In conclusion, increasing the ECal inner radius benefits the jet energy resolution because it increases the separation between particles as they enter the calorimeter, which reduces confusion.

2.5 Summary

The effect of varying the configuration of the calorimeters, the magnetic field strength and the overall detector size on the single particle and jet energy resolutions were presented in this chapter. For both the ECal and the HCal, the dominant factor determining the intrinsic energy resolution was the longitudinal sampling frequency. However, the jet energy resolution had the strongest sensitivity to the ECal cell size, which shows that spatial recognition is more important when using particle flow calorimetry than intrinsic energy resolution. The HCal cell size was found to be less significant than the ECal cell size for determining the jet energy resolution because separation of nearby particle showers in the HCal uses the spatial information gathered in the ECal. In the particle flow paradigm, fine segmentation in the ECal can compensate for the coarser HCal granularities. The jet energy resolution also showed a strong dependence on the magnetic field strength and the overall detector size. Increasing both the magnetic field and overall detector size leads to greater separation of nearby particle showers in the calorimeters, which reduces the effect of confusion.

Colophon

This thesis was made in $\text{\LaTeX} 2_{\varepsilon}$ using the “hepthesis” class [\[21\]](#).

Bibliography

- [1] Halina Abramowicz et al. The International Linear Collider Technical Design Report - Volume 4: Detectors. 2013.
- [2] Lucie Linssen, Akiya Miyamoto, Marcel Stanitzki, and Harry Weerts. Physics and Detectors at CLIC: CLIC Conceptual Design Report. 2012.
- [3] C. W. Fabjan and F. Gianotti. Calorimetry for particle physics. *Rev. Mod. Phys.*, 75:1243–1286, 2003.
- [4] M. A. Thomson. Particle Flow Calorimetry and the PandoraPFA Algorithm. *Nucl. Instrum. Meth.*, A611:25–40, 2009.
- [5] M. Derrick, D. Gacek, N. Hill, B. Musgrave, R. Noland, E. Petereit, J. Repond, R. Stanek, and K. Sugano. Design and construction of the ZEUS barrel calorimeter. *Nucl. Instrum. Meth.*, A309:77–100, 1991.
- [6] Huong Lan Tran, Katja Krüger, Felix Sefkow, Steven Green, John Marshall, Mark Thomson, and Frank Simon. Software compensation in Particle Flow reconstruction. 2017.
- [7] R. Wigmans. Calorimetry: Energy measurement in particle physics. *Int. Ser. Monogr. Phys.*, 107:1–726, 2000.
- [8] L. Landau. On the energy loss of fast particles by ionization. *J. Phys.(USSR)*, 8:201–205, 1944.
- [9] H. Bichsel, Donald E. Groom, and S. R. Klein. Passage of particles through matter. 2004.
- [10] Oskar Hartbrich. AHCAL Digitisation. CALICE Spring Meeting 2015 & LCWS 2015, Tsukuba (Japan), 19 Apr 2015 - 24 Apr 2015, Apr 2015.
- [11] C. Adloff et al. Hadronic energy resolution of a highly granular scintillator-steel

- hadron calorimeter using software compensation techniques. *JINST*, 7:P09017, 2012.
- [12] C. Adloff et al. The Time Structure of Hadronic Showers in highly granular Calorimeters with Tungsten and Steel Absorbers. *JINST*, 9:P07022, 2014.
- [13] Toshinori Abe et al. The International Large Detector: Letter of Intent. 2010.
- [14] C. Patrignani et al. Review of Particle Physics. *Chin. Phys.*, C40(10):100001, 2016.
- [15] J. B. Birks. Scintillations from Organic Crystals: Specific Fluorescence and Relative Response to Different Radiations. *Proc. Phys. Soc.*, A64:874–877, 1951.
- [16] M. Chefdeville et al. Shower development of particles with momenta from 15 GeV to 150 GeV in the CALICE scintillator-tungsten hadronic calorimeter. *JINST*, 10(12):P12006, 2015.
- [17] G. Folger and J. P. Wellisch. String parton models in GEANT4. *eConf*, C0303241:MOMT007, 2003.
- [18] *Geant4 Physics Reference Manual, Section IV, Chapter 28*.
- [19] M. P. Guthrie, R. G. Alsmiller, and H. W. Bertini. Calculation of the capture of negative pions in light elements and comparison with experiments pertaining to cancer radiotherapy. *Nucl. Instrum. Meth.*, 66:29–36, 1968.
- [20] A. Caldwell, L. Hervas, J. A. Parsons, F. Sciulli, W. Sippach, and L. Wai. Measurement of the time development of particle showers in a uranium scintillator calorimeter. *Nucl. Instrum. Meth.*, A330:389–404, 1993.
- [21] Andy Buckley. The hepthesis L^AT_EX class.